



OPEN Fault diagnosis of permanent magnet synchronous motor based on MTF fusion image and NRBO-SCN method

Yinquan Yu^{1✉}, Hongping Ge^{2,4}, Giuseppe Carbone³, Dequan Zeng¹, Yiming Hu¹ & Jinwen Yang¹

To address the limitations of conventional feature extraction methods in capturing fault information from operational current signals, the paper proposes a novel fault diagnosis method for permanent magnet synchronous motor (PMSM). The approach integrates markov transition field (MTF) image fusion, a newton raphson based optimization(NRBO), and a stochastic configuration network (SCN). Firstly, a high-fidelity simulation model of the PMSM is developed, and the three-phase current signals are extracted as the effective fault indicators. Secondly, the three-phase current signals are transformed into two-dimensional MTF images, which are then fused into RGB images. Thirdly, extract the color, shape and texture features of MTF fused images separately to construct feature vectors of fault information. Finally, to enhance classification accuracy, the SCN model is optimized using the NRBO algorithm, improving its generalization and fault identification capabilities. The extracted fault feature vectors are then input into the NRBO-SCN model for fault identification. By collecting actual PMSM fault diagnosis data for verification, compared with other fault classification methods, the proposed method in this paper has superior fault classification performance and can accurately identify the fault types of the PMSM eccentricity and demagnetization.

Keywords Permanent magnet synchronous motor, Markov transition field, Newton raphson based optimization, Stochastic configuration network, Fault diagnosis

PMSM have the advantages of simple structure, reliable operation, high efficiency, and easy control, and are widely used in applications such as new energy vehicles, industrial automation, and aerospace¹. However, PMSM will inevitably fail during long periods of operation due to improper operation, harsh environments, and aging materials, which will affect its operational efficiency and reliability². Therefore, accurately diagnosing PMSM faults is of great practical significance in reducing the risk of accidents³.

When a fault occurs in the PMSM, fault-related information will be generated in various physical signals represented by vibration, acoustic noise, stator current, and voltage. Physical quantities characterizing the state of the motor can be obtained by extracting features from signals. The PMSM stator current signal has the advantages of easy acquisition and non-intrusive, so it is widely used in motor fault detection. Traditional fault diagnosis methods based on one-dimensional data processing require high prior knowledge and complex feature extraction processes, which leading to a certain degree of limitation in the field of fault diagnosis. Therefore, with the continuous development of image processing technology, many scholars convert one-dimensional signals into images and realize the extraction of different types of fault features through image processing, which provide a remarkably new way in the field of fault diagnosis. Fan et al.⁴ transformed the collected signal into a two-dimensional time-frequency waveform by employing wigner-ville distribution (WVD) and extracted energy profile values in the time-frequency waveform to characterize the rolling bearing fault types, which achieves the identification of different faults in the rolling bearings. Pietrzak et al.⁵ applied short-time fourier transform(STFT) to dig demagnetization fault features from the stator phase current signal of the PMSM, and demonstrated the high reliability of the proposed approach through experimental data. Halder et al.⁶ applied

¹School of Mechatronics and Vehicle Engineering, East China Jiaotong University, Nanchang 330013, China. ²School of Transportation Engineering, East China Jiaotong University, Nanchang 330013, China. ³Department of Mechanical, Energy, and Management Engineering, University of Calabria, Rende 87036, Italy. ⁴Science and Technology College of Nanchang Hangkong University, Gongqingcheng 332020, China. ✉email: yu_yinquan@ecjtu.edu.cn

continuous wavelet transform to the current signal of induction motors, and verified through finite element simulation data that continuous wavelet transform can accurately express the characteristics of rotor broken strip faults in induction machines in the time-frequency field. El-Dalahmeh et al.⁷ used the Hilbert-Huang transform (HHT) in the PMSM fault feature extraction, and experimental data validation showed that the HHT can realize the fault state monitoring of the PMSM under various working states. Although the mentioned time-frequency analysis algorithms have accomplished effective fault diagnosis, the time-frequency waveform cannot reflect the complete information of the original signal and is susceptible to the influence of human experience.

To overcome the aforementioned drawbacks, image transformation techniques such as gram angle field (GAF), symmetrized dot pattern (SDP), recurrence plot (RP), and markov transfer field (MTF) can effectively avoid the loss of one-dimensional signal information when reconstructing the data and retain the correlation with time, which are widely used in the domain of fault detection. Zhang et al.⁸ converted the acquired one-dimensional torque signal of the PMSM into a two-dimensional image by means of the GAF, and effectively achieved various categories of demagnetization fault detect through the actual torque signal of the PMSM. Yuan et al.⁹ converted the collected PMSM current signals into the SDP images with color information, and effectively identified the fault state of the motor using the two-dimensional convolutional neural network, and attained a high fault diagnosis precision rate. Jiang et al.¹⁰ converted the bearing vibration signal into the two-dimensional graph with defective characteristics by RP method. The actual rolling bearing fault experimental data showed that the RP approach can successfully dig the hidden defective features in the vibration signal and has a better fault diagnosis capability. Lei et al.¹¹ used MTF to convert one-dimensional vibration signals of rolling bearings into two-dimensional graph, and verified the strong fault classification performance of MTF in the domain of fault classification using actual rolling bearing experimental signal. MTF method effectively preserves both the temporal dependence of the original signal and its frequency characteristics, effectively preventing the loss of fault feature information. It has good visual quality and is widely used in the field of fault diagnosis.

The essence of fault feature classification is to input the fault feature information into the classifier to identify its fault type. Existing fault diagnosis methods usually use support vector machine (SVM)^{12,13}, ConvNext model^{14,15}, ResNet model^{16,17}, and extreme learning machine (ELM)^{18,19} as fault classifiers to efficiently identify different fault types. Wu et al.²⁰ used SVM to classify PMSM fault states, and experimental data verification showed that the presented scheme can correctly detect open circuit problems in six phase PMSM power transmission system. Xing et al.²¹ combined transfer learning with ConvNext model for fault diagnosis of rotating machinery, effectively solving the problem of fault diagnosis of small sample rotating machinery. Wei et al.²² applied the ResNet method to the PMSM and effectively achieved online diagnosis of inter turn short circuit faults in the PMSM. Xu et al.²³ adopted ELM to achieve fault detection in microgrids, and the proposed method has faster learning speed and higher learning accuracy compared to other methods. Although the above fault classification methods have achieved good diagnostic results, issues such as complex selection of hyperparameters, vulnerability to partial optimization, and sluggish training speeds have limited the scope of application.

As the latest model of random parameter neural networks, the stochastic configuration network (SCN)²⁴ has the benefits of fewer parameter settings, shorter training time, and faster convergence speed in processing large-scale and high-dimensional data due to its excellent supervision mechanism and incremental network model. Due to its solid theoretical support and efficient modeling architecture, SCN method has a promising application in the field of the fault monitoring. However, the properties of the SCN is influenced by the regularization factor r and the scaling factor λ . Different parameter selection leads to different learning abilities of the SCN models, therefore, finding the optimal combination of parameters is crucial for the modeling speed and generalization performance of the SCN method. The commonly used intelligent optimization algorithms include snake optimization (SO)^{25,26}, dung beetle optimizer (DBO)^{27,28}, rime optimization algorithm (RIME)^{29,30}, crested porcupine optimization (CPO)^{31,32}, and newton raphson based optimizer (NRBO)^{33,34}. The NRBO algorithm is a new meta-heuristic algorithm with advantages such as fast search speed, less susceptibility to local optima, and good robustness than other conventional intelligent optimization algorithms. The article attempts to optimize the parameters of the SCN using the NRBO optimization method to fully leverage the capabilities of the fault classifiers.

In summary, a PMSM fault detect approach based on MTF fusion image and NRBO-SCN is presented to address the issue of low diagnostic accuracy due to insufficient feature extraction capability of PMSM current signal. The method combines the excellent visual quality of MTF in terms of images and the superior fault classification performance of SCN, and effectively achieves demagnetization and eccentricity fault diagnosis of PMSM. The contributions of the paper are summarized in the following three aspects.

- (1) The one-dimensional three-phase current signals are transformed into two-dimensional MTF images and fused into a single composite image. This process enriches the fault feature information by visualizing the temporal correlation of the signals through RGB color channels, thereby providing a more information-dense representation for feature extraction.
- (2) The color, shape, and texture features are systematically extracted from the fused MTF image to construct the comprehensive fault feature vector. This process captures the global characteristics of different faults, thereby generating a more discriminative feature set for subsequent fault identification.
- (3) The NRBO algorithm is employed to automatically optimize the key parameters of the SCN classifier. This approach eliminates the need for manual tuning, significantly enhances the model convergence speed, and achieves high fault diagnosis accuracy.

The remainder of the paper is organized as follows. “Theoretical studies” describes the theoretical foundation of the proposed method. “Design of fault diagnosis model based on MTF-NRBO-SCN” mainly elaborates the steps

of the design of fault diagnosis model based on MTF-NRBO-SCN. “Proposed method validation” validates the effectiveness and superiority of the presented approach through the PMSM simulation model and experimental platform datasets, and compares it with other methods. “Conclusions” summarizes the whole paper and provides conclusions.

Theoretical studies

MTF theory

The fundamental concept of the MTF approach is to realize the way of encoding dynamic transfer information through markov transfer probability. MTF method converts one-dimensional time signal into two-dimensional graph with good visual effects. Assuming the collected time series is $S = \{s_1, s_2, \dots, s_N\}$, the MTF method encoding process is as follows.

- (1) Discretize the range of values of one-dimensional time series $S = \{s_1, s_2, \dots, s_N\}$ into Q intervals. Quantify all values of the time series using the quantile interval q_j ($0 < j \leq Q$).
- (2) By identifying quantile intervals and mapping each s_i to a unique corresponding q_j . Constructing a $Q \times Q$ weighted adjacency matrix W by calculating the transfer probabilities between each q_i . The expression for the matrix W is shown in Eq. (1).

$$W = \begin{bmatrix} w_{11} & w_{12} & \cdots & w_{1Q} \\ w_{21} & w_{22} & \cdots & w_{2Q} \\ \vdots & \vdots & \vdots & \vdots \\ w_{Q1} & w_{Q2} & \cdots & w_{QQ} \end{bmatrix} \quad (1)$$

Where w_{ij} express the probability that data in interval q_i is followed by interval q_j , and $w_{ij} = P(s_t \in q_i | s_{t-1} \in q_j)$.

- (3) Expand the markov transfer matrix W into an $N \times N$ markov variation field M by aligning every probe according to the temporal sequence. The expression for matrix M is shown in Eq. (2).

$$M = \begin{bmatrix} m_{11} & m_{12} & \cdots & m_{1n} \\ m_{21} & m_{22} & \cdots & m_{2n} \\ \vdots & \vdots & \vdots & \vdots \\ m_{n1} & m_{n2} & \cdots & m_{nn} \end{bmatrix} \quad (2)$$

Where m_{ij} is the transition probability from interval q_i to interval q_j , and $m_{ij} = P(s_i \in q_i \rightarrow s_j \in q_j)$.

The MTF method encodes the acquired one-dimensional signal in the form of two-dimensional feature mapping by the above method, so that each pixel point in the two-dimensional image not only contains the values of each element of the one-dimensional signal, but also preserves the relevant features of the time signal to the maximum extent. The MTF method can adequately represent the fault features of the initial signal in the form of images.

NRBO algorithm

The NRBO algorithm adopts the newton raphson search rule(NRSR) to improve search capability and accelerate convergence speed, and introduces the trap avoidance operator(TAO) to avoid local optimal traps. The detailed procedure is as follows.

- (1) Population initialization. For a population with a given number of N_p individuals, it is assumed that the parameters to be optimized have dim dimensions. The initial position of the random population is generated using Eq. (3).

$$x_{nj} = lb + rand(up - lb) \quad (3)$$

Where x_{nj} is the location of the n th individual in the j th dimension, $j \in [1, dim]$, $n \in [1, N_p]$. lb and up respectively represent the lower and upper limits of the optimization parameters. $rand$ is the arbitrary value between (0, 1).

- (2) Calculate the initial fitness value. According to the predefined fitness function, the adaptation value of every sample is solved. The best and the worst fitness values and the corresponding positions x_b and x_w are filtered out.
- (3) Updating the optimal solution based on NRSR rules. Explore the location of the n th individual in the t -th iteration using the NRSR method. The new position is expressed utilizing Eq. (4).

$$x_n^{t+1} = r_1[r_1 X 1_n^t + (1 - r_2) X 2_n^t] + (1 - r_2) X 3_n^t \quad (4)$$

Where x_n^{t+1} is the location updated based on NRSR rules. t and n respectively express the value of iterations and individual number. r_1 and r_2 respectively indicate random numbers between (0, 1). $X 1_n^t$, $X 2_n^t$, and $X 3_n^t$ indicates the NRBO algorithm, which iteratively updates the current position to obtain three new positions in order to enhance local and overall search performance. The calculations for three positions are shown in Eqs. (5)–(7).

$$X1_n^t = x_n^t - Nr + Rho \tag{5}$$

$$X2_n^t = x_b - Nr + Rho \tag{6}$$

$$X3_n^t = x_n^t - \delta(X2_n^t - X1_n^t) \tag{7}$$

Where Nr express the value obtained through the NRSR search rule. x_b express the current best position. Rho is the step factor that leads the population in the correct orientation. δ is an adaptive parameter that varies with the number of iterations, and it is employed to prevent slipping into a local optimal and to reduce the amount of computation.

Based on the above population search approach, the search process of NRSR is shown in Eqs. (8)–(11).

$$NRSR = randn \frac{(y_w - y_b)\Delta x}{2(y_w + y_b - 2x_n^t)} \tag{8}$$

$$Rho = a(x_b - x_n^t) + b(x_{a_1}^t - x_{a_2}^t) \tag{9}$$

$$\delta = (1 - \frac{2t}{T})^5 \tag{10}$$

$$\Delta x = randn |x_b - x_n^t| \tag{11}$$

Where y_w and y_b are the two positions obtained through the NRSR search rule, which are used to improve the search performance of the NRBO method. Δx express search scope. a and b respectively represent the arbitrary values in the middle of (0, 1). a_1 and a_2 respectively indicate two random numbers that are different from each other between $[1, Np]$. T is the maximum value of iterations.

- (4) Trap avoidance operator(TAO). The purpose of the TAO algorithm is to improve the effectiveness of the NRBO approach in computing real engineering problems and to prevent slipping into local best solutions. If the value of $rand$ is less than DF (the value of DF is usually 0.6), the value of X_{TAO}^{IT} is obtained by the calculation of Eqs. (12)–(13).

$$\begin{cases} X_{TAO}^{IT} = X_n^{IT+1} + \theta_1 \times (\mu_1 \times x_b - \mu_2 \times X_n^{IT}) + \theta_2 \times \delta \\ \quad \times (\mu_1 \times Mean(X^{IT}) - \mu_2 \times X_n^{IT}), \mu_1 < 0.5 \\ X_{TAO}^{IT} = x_b + \theta_1 \times (\mu_1 \times x_b - \mu_2 \times X_n^{IT}) + \theta_2 \times \delta \\ \quad \times (\mu_1 \times Mean(X^{IT}) - \mu_2 \times X_n^{IT}), \mu_1 \geq 0.5 \end{cases} \tag{12}$$

$$X_n^{IT+1} = X_{TAO}^{IT} \tag{13}$$

Where θ_1 and θ_2 respectively denote arbitrary number between $(-1, 1)$ and $(-0.5, 0.5)$. DF represent an important parameter for controlling NRBO performance. μ_1 and μ_2 respectively indicate arbitrary number, which are calculated as shown in Eqs. (14)–(15).

$$\mu_1 = \beta \times 3 \times rand + (1 - \beta) \tag{14}$$

$$\mu_2 = \beta \times rand + (1 - \beta) \tag{15}$$

Where the value of β is 0 or 1. If the random number $\Delta \geq 0.5$, then $\beta = 0$, otherwise $\beta = 1$. Due to the randomness of the values of factors μ_1 and μ_2 , the sample population becomes more diverse. It can avoid local optimal and also increase diversity.

Working principle of the SCN

SCN method is an emerging incremental neural network model with good approximation and generalization properties. The fundamental concept of SCN approach is to start from a smaller network and incrementally generate hidden layer nodes based on training sample data to construct a network structure model. The basic structural model of SCN is shown in Fig. 1.

Assuming training samples $X = \{x_1, x_2, \dots, x_n\}$, where $x_i = [x_{i,1}, x_{i,2}, \dots, x_{i,d}] \in R^d, i = 1, 2, \dots, n$. Set label $Y = \{y_1, y_2, \dots, y_n\}$, where $y_i = [y_{i,1}, y_{i,2}, \dots, y_{i,m}] \in R^m$. The detailed calculation procedure is as follows.

- (1) Assuming that $L-1$ hidden layer nodes have been constructed, the current network output model is shown in Eq. (16).

$$f_{L-1}(X) = \sum_{j=1}^{L-1} \beta_j \varphi(w_j^T X + b_j), f_0 = 0 \tag{16}$$

Where β_j represents the output weight of hidden level node i . φ indicate the calibration function.

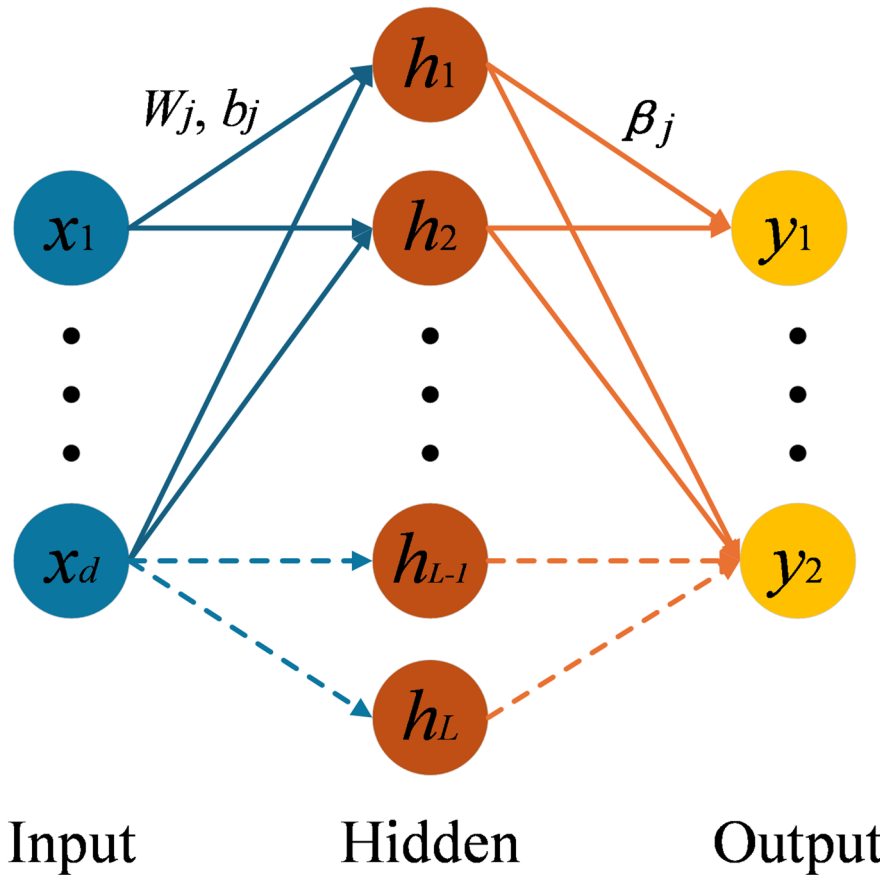


Fig. 1. Basic structural model diagram of SCN.

(2) The residual definition of SCN algorithm is shown in Eq. (17).

$$E_{L-1} = Y - f_{L-1}(X) = [E_{L-1,1}(X), E_{L-1,2}(X), \dots, E_{L-1,m}(X)] \tag{17}$$

(3) If $\|E_{L-1}\|$ does not satisfied the preset error or the maximum value of hidden horizon nodes L_{max} is not reached, then a fresh hidden node needs to be created by point increment under the supervision mechanism. The node parameters are randomly generated by Eqs. (18)–(19). When Eq. (22) is satisfied, the input weights and hidden layer offsets corresponding to the time when Eq. (21) is maximized by the supervisory mechanism Eq. (20) are treated as the configuration parameters of the hidden horizon nodes of the current model.

$$w_j = \lambda \times (2 \times rand(d, L) - 1) \tag{18}$$

$$b_j = \lambda \times (2 \times rand(1, L) - 1) \tag{19}$$

$$h_L = [\varphi(w_L^T x_1 + b_L), \dots, \varphi(w_L^T x_N + b_L)]^T \in R^N \tag{20}$$

$$\xi_{L,j} = \frac{(E_{L-1,j}^T \times h_L)^2}{h_L^T h_L} - (1 - r - \mu_L) \|E_{L-1,j}\|_F^2 \tag{21}$$

$$\xi_L = \sum_{j=1}^m \xi_{L,j} \geq 0 \tag{22}$$

Where r denotes the regularization factor, $r \in [0, 1]$. μ_L denote a sequence of non- negative real numbers, $\lim_{L \rightarrow \infty} \mu_L = 0, \mu_L \leq 1 - r$.

(4) By calculating the optimal output weight, the calculation of the optimal output weight is shown in Eq. (23).

$$\beta^* = \arg \min_{\beta} \|H_L \beta - Y\|_F^2 = H_L^\dagger Y \tag{23}$$

Where H_L^\dagger represent Moore-Penrose generalized inverse matrix H_L , $\|\cdot\|_F$ represents the Frobenius norm.

(5) The final output of the SCN network is shown in Eq. (24).

$$f = H\beta^* \tag{24}$$

Image feature extraction

Color feature extraction

Due to the fact that the color information of an image is mainly distributed in low order moments, using the three moments of the image can enrich the characterization of the color distribution of the image. The three color moments of the three color components R, G, and B in the image form nine-dimensional feature vector. The first-order moment mainly reflects the brightness of the image. The second-order moment mainly reflects the range of image color distribution. The third-order moments reflect the symmetry of the image color distribution. The mathematical expressions are shown in Eqs. (25)–(27).

$$u_i = \frac{1}{N} \sum_{j=1}^N p_{ij} \tag{25}$$

$$\sigma_i = \left[\frac{1}{N} \sum_{j=1}^N (p_{ij} - \mu_i)^2 \right]^{\frac{1}{2}} \tag{26}$$

$$\zeta_i = \left[\frac{1}{N} \sum_{j=1}^N (p_{ij} - \mu_i)^3 \right]^{\frac{1}{3}} \tag{27}$$

Where p_{ij} represent the i -th color element of the j -th pixel. N represent the value of pixels in the research image.

Shape feature extraction

Hu invariant moment is a statistical measure employed to represent image shape feature vectors, which has translation, rotation, and scale invariance. The calculation process is as follows.

(1) In the continuous image, the graph function is defined as $f(x, y)$, and the calculation process of the $(p + q)$ geometric moment m_{pq} and central moment μ_{pq} of the graph is shown in Eqs. (28)–(29).

$$m_{pq} = \sum_{x=1}^N \sum_{y=1}^M x^p y^q f(x, y) \tag{28}$$

$$\mu_{pq} = \sum_{x=1}^N \sum_{y=1}^M (x - x_0)^p (y - y_0)^q f(x, y) \tag{29}$$

Where $p, q = 0, 1, 2, \dots, N$ and M respectively denote the value of rows and columns in the graph. $x_0 = m_{10}/m_{00}, y_0 = m_{01}/m_{00}$.

(2) The central moment μ_{pq} is normalized and calculated as shown in Eq. (30).

$$\eta_{pq} = \frac{\mu_{pq}}{\mu_{00}^\gamma} \tag{30}$$

Where μ_{00} denote the zero-order central moment, $\gamma = \frac{p+q+2}{2}, p + q = 2, 3, \dots$.

(3) Construct seven Hu invariants, and the calculation process is shown in Eqs. (31)–(37).

$$\varphi_1 = \eta_{20} + \eta_{02} \tag{31}$$

$$\varphi_2 = (\eta_{20} - \eta_{02})^2 + 4\eta_{11}^2 \tag{32}$$

$$\varphi_3 = (\eta_{30} - 3\eta_{12})^2 + (3\eta_{21} - \eta_{03})^2 \tag{33}$$

$$\varphi_4 = (\eta_{30} + \eta_{12})^2 + (\eta_{03} + \eta_{21})^2 \tag{34}$$

$$\begin{aligned} \varphi_5 = & (\eta_{30} - 3\eta_{12})(\eta_{30} + \eta_{12}) [(\eta_{30} + \eta_{12})^2 - 3(\eta_{21} + \eta_{03})^2] \\ & + (3\eta_{21} - \eta_{03})(\eta_{21} + \eta_{03}) \cdot [3(\eta_{30} + \eta_{12})^2 - (\eta_{03} + \eta_{21})^2] \end{aligned} \tag{35}$$

$$\varphi_6 = (\eta_{20} - \eta_{02}) [(\eta_{30} + \eta_{12})^2 - (\eta_{03} + \eta_{21})^2] + 4\eta_{11} (\eta_{30} + \eta_{12}) (\eta_{03} + \eta_{21}) \tag{36}$$

$$\begin{aligned} \varphi_7 = & (3\eta_{21} - \eta_{03}) (\eta_{30} + \eta_{12}) [(\eta_{30} + \eta_{12})^2 - 3(\eta_{21} + \eta_{03})^2] \\ & + (3\eta_{21} - \eta_{30}) (\eta_{03} + \eta_{21}) [3(\eta_{30} + \eta_{12})^2 - (\eta_{21} + \eta_{03})^2] \end{aligned} \tag{37}$$

Tamura texture feature extraction

The tamura texture feature contains six feature attributes that effectively express image texture information.

- (1) Roughness F_{coa} . Roughness indicates the granularity size of the faulty image texture patterns, and the calculation process is shown in Eqs. (38)–(39).

$$F_{coa} = \frac{1}{m \times n} \sum_{h=i-1}^{i+1} \sum_{\omega=j-1}^{j+1} S_{best} \tag{38}$$

$$\begin{cases} S_{best} = \max \{E_{n,m}(i, j) | n \in [1, 5], m = \mu, \nu\} \\ E_{k,u}(x, y) = |A_k(x + 2^{k-1}, y) - A_k(x - 2^{k-1}, y)| \\ E_{k,\nu}(x, y) = |A_k(x, y + 2^{k-1}) - A_k(x, y - 2^{k-1})| \\ A_k(x, y) = \sum_{i=x-2^{k-1}}^{x+2^{k-1}-1} \sum_{j=y-2^{k-1}}^{y+2^{k-1}-1} \frac{g(i, j)}{2^{2k}}, k = 0, 1, 2, \dots, 5 \end{cases} \tag{39}$$

Where $E_{k,u}(x, y)$ denotes the mean grayscale variance of the graph pixels in the horizontal orientation. $E_{k,\nu}(x, y)$ denotes the mean grayscale variance of the image pixels in the vertical direction. $A_k(x, y)$ indicate the mean intensity within the activity window. $g(i, j)$ represent the grayscale number of an image. m and n respectively indicate the length and width of the studied image.

- (2) Directionality F_{dir} . Directionality represent the form in which pixels in a graph appear in the particular orientation. The calculation process is shown in Eqs. (40)–(41).

$$F_{dir} = |d(x, y) - \mu(x, y)| \tag{40}$$

$$\begin{cases} d(x, y) = \begin{cases} 0, & |\Delta G(k, h, \omega)| < t \\ \theta(x, y), & |\Delta G(k, h, \omega)| \geq t \end{cases} \\ \mu(x, y) = \frac{1}{9} \sum_{i=1}^{i+1} \sum_{j=1}^{j+1} d(i, j) \\ |\Delta G(x, y)| = (|\Delta_H| + |\Delta_V|) / 2 \\ \theta = \arctan(\Delta_V / \Delta_H) + \pi / 2 \end{cases} \tag{41}$$

Where $d(x, y)$ indicate direction angle, $\mu(x, y)$ denote the mean number corresponding to the orientation angle in the neighborhood. Δ_H, Δ_V respectively represent the amount of change in the gradient in the horizontal and vertical orientation of the image.

- (3) Contrast F_{con} . Contrast represent the variation of image grayscale. The computation procedure is shown in Eq. (42).

$$F_{con} = \sigma a_4^{-1/4} \tag{42}$$

Where $a_4 = \mu_4 / \sigma^4, \mu_4$ denote the 4-th order moment, σ represent variance.

- (4) Linearity F_{lin} . Linearity indicate the degree of deviation of the distance between the intervals of the image pixels. The calculation process is shown in Eq. (43).

$$F_{lin} = \frac{\sum_{i=1}^m \sum_{j=1}^m P_a(i, j) \cos [(i - j) \frac{2\pi}{n}]}{\sum_{i=1}^m \sum_{j=1}^m P_a(i, j)} \tag{43}$$

Where P_a indicate the distance point of the covariance matrix in the local direction of $m \times m$.

- (5) Regularity F_{reg} . Regularity indicate the degree of image texture regularity. The calculation process is shown in Eq. (44).

$$F_{reg} = 1 - r(\sigma_{coa} + \sigma_{con} + \sigma_{dir} + \sigma_{lin}) \tag{44}$$

Where r represent normalization factor. $\sigma_{coa}, \sigma_{con}, \sigma_{dir}, \sigma_{lin}$ denote the standard deviation of each corresponding texture feature parameter.

(6) Roughness F_{rou} . Roughness indicate the degree of roughness of the image. The calculation process is shown in Eq. (45).

$$F_{rou} = F_{coa} + F_{con} \tag{45}$$

Design of fault diagnosis model based on MTF-NRBO-SCN Performance analysis of NRBO algorithm

To comprehensively verify the optimization capability of NRBO, six criteria test functions are selected and contrasted by experimental analysis with SO approach, DBO approach, RIME approach and CPO approach. The specific information of the six testing functions is shown in Table 1.

The selected testing function has nonlinearity and multimodality, which facilitates comprehensive testing of the capability of optimization approaches. The F1 and F2 functions are single-peak test functions employed to test the convergence rates and solution precision of the algorithm. The F3 and F4 functions are multi-peak test functions intended to test the algorithm capability to search globally and to skip local optimal. The F5 and F6 functions are composite test functions employed to test the combined ability of the approach for global development and local exploration. In order to guarantee the equality of the compared optimization algorithms, a standardized setting is adopted, which sets the population size to 30 and the maximum value of iterations to 500. Every approach was automatically repeated 30 times.

Convergence analysis

The convergence curve of the algorithm can intuitively demonstrate the optimization accuracy and convergence efficiency of the approach. The convergence analysis results of the approach are shown in Fig. 2. By observing Fig. 2a, b, it can be seen that the optimization speed of the NRBO algorithm reduces exponentially. Compared with other algorithms, NRBO algorithm has superior fast optimization ability. By observing Fig. 2c, d, it can be clearly indicated that compared with other approaches, the NRBO algorithm approaches the optimal solution at the initial iteration time and has higher convergence accuracy and stability. From Fig. 2e, f, it is evident that the NRBO algorithm maintained excellent performance throughout the entire iteration process. The NRBO algorithm not only avoids the problem of local optimal, but also successfully searches for the optimal fitness

Functions	Dimension (Dim)	Range	F_{min}
$F1(x) = \sum_{i=1}^n x_i^2$	30	[-100,100]	0
$F2(x) = \sum_{i=1}^n (\sum_{j=1}^i x_j)^2$	30	[-100,100]	0
$F3(x) = -20 \exp(-0.2 \sqrt{\frac{1}{n} \sum_{i=1}^n x_i^2}) - \exp(\frac{1}{n} \sum_{i=1}^n \cos 2\pi x_i) + 20 + e$	30	[-32,32]	0
$F4(x) = \frac{\pi}{n} \{10\sin^2(\pi y_i) + \sum_{i=1}^{n-1} (y_i - 1)^2 [1 + 10\sin^2(\pi y_{i+1})] + (y_n - 1)^2\} + \sum_{i=1}^n u(x_i, 10, 100, 4)$ $y_i = 1 + \frac{1}{4}(x_i + 1)$ $u(x_i, a, k, m) = \begin{cases} k(x_i - a)^m, & x_i > a \\ 0, & -a \leq x_i \leq a \\ k(-x_i - a)^m, & x_i < -a \end{cases}$	30	[-50,50]	0
$F5(x) = \sum_{i=1}^{11} \left[a_i - \frac{x_1(b_i^2 + b_i x_2)}{b_i^2 + b_i x_3 + x_4} \right]^2$	4	[-5,5]	0.0003075
$F6(x) = - \sum_{i=1}^{10} [(x - a_i)(x - a_i)^T + c_i]^{-1}$	4	[0,10]	-10

Table 1. The specific information of test functions.

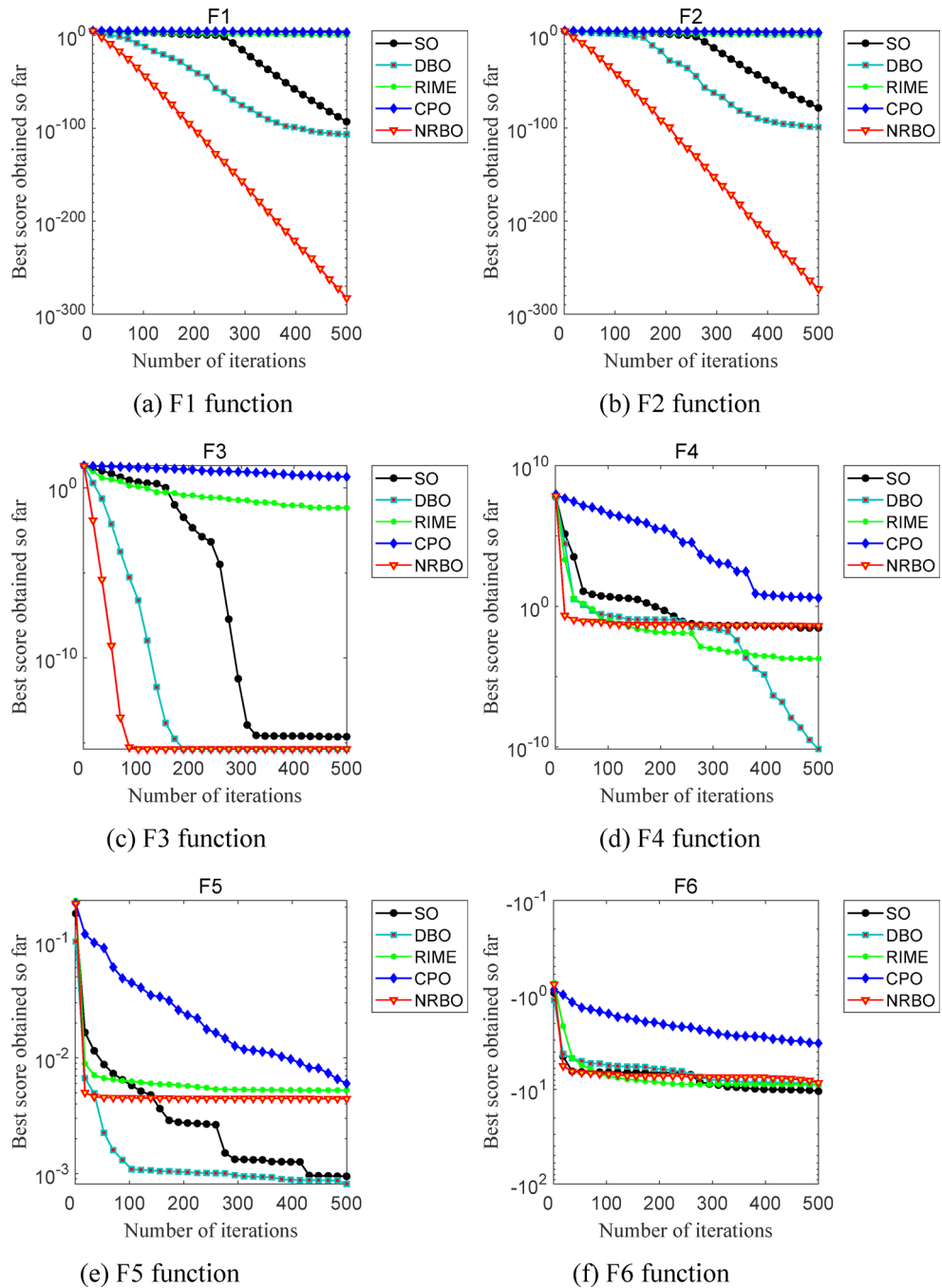


Fig. 2. Comparative results of convergence of NRBO algorithm.

value. Based on the above discussion, it can be observed that the NRBO technique has significant advantages in terms of optimization performance compared to other algorithms.

Stability analysis

The box plot can visually display the central trend, dispersion, and outlier situation of data. The box plot results of five algorithms in different test functions is shown in Fig. 3. From Fig. 3a–f, it can be seen that there are very few outlier points in the NRBO algorithm, and the data sample points are clustered around the average value. However, the distribution of data sample points in other optimization algorithms is relatively chaotic, and many outlier points have appeared. In summary, the NRBO algorithm did not experience significant fluctuations in the test function, and its box plot was the smallest and most stable, demonstrating good robustness.

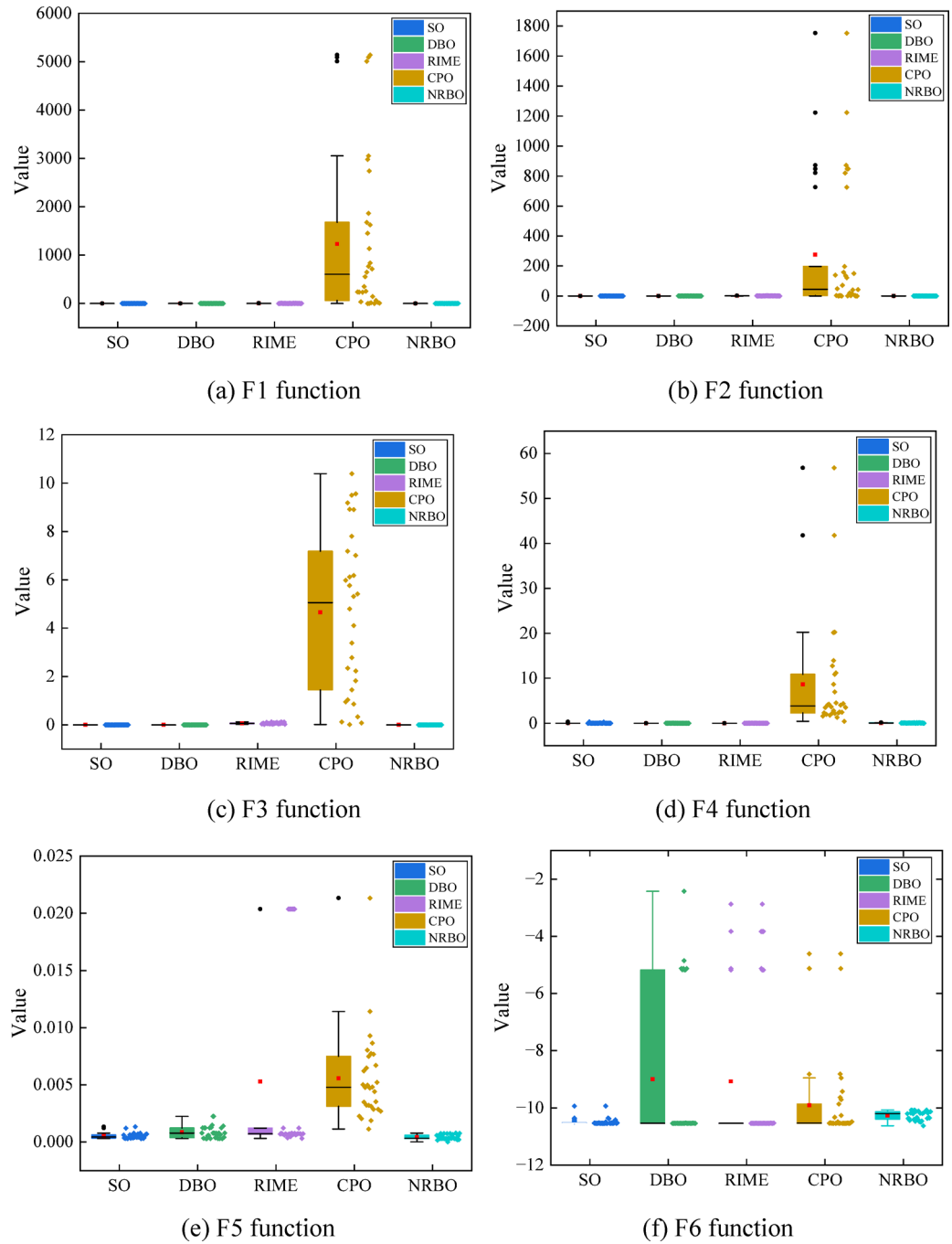


Fig. 3. Stability analysis results of NRBO algorithm.

NRBO-SCN model process

The regularization factor r and scaling factor λ in the SCN algorithm seriously influence the diagnostic properties of the fault detect approach. The choice of regularization parameter r affect the degree of contraction of the supervision mechanism, while the choice of scaling factor λ affect the search efficiency of network parameters. Therefore, the article adopts the NRBO algorithm to adaptively select SCN model parameters. The flowchart of NRBO-SCN is depicted in Fig. 4, and the specific procedures are as follows.

- (1) Set the parameters of SCN algorithm. Maximum value of hidden layer nodes L_{max} , maximum value of candidate nodes T_{max} , residual value ϵ , range of regularization parameters $r \in [0.9, 0.999999]$, range of scaling factors $r \in [0.5, 100]$. Set the parameters of the NRBO approach. Population size Np , maximum iteration coefficient max_IT , decision factor DF , The upper and lower bounds $[up, lp]$ and dimensions of the search space. Randomly initialize individual populations using the upper and lower bounds and dimensions of the search space as boundaries.

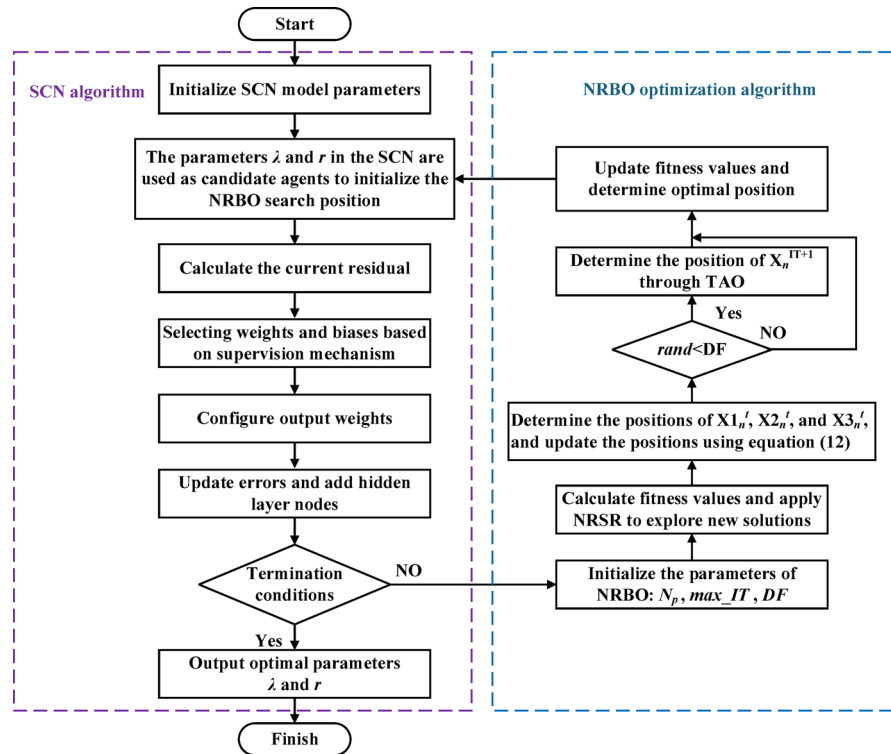


Fig. 4. The flowchart based on NRBO-SCN model.

- (2) Build the NRBO-SCN model and calculate fitness values. Select the classification accuracy of the sample as the fitness function, and the calculation process of the fitness function is depicted in Eq. (46).

$$f(x^t) = accuracy(\lambda, r) = \frac{y_T}{y_T + y_F} \quad (46)$$

Where y_T indicate the correct sample, y_F indicate the wrong sample.

- (3) Execute NRBO search algorithm. By using Eq. (46) to update the search position, the fitness value can be updated to optimize the parameters r and λ in the SCN algorithm.
- (4) Judging termination criteria. When the tolerance error is reached, the iteration terminates and the final parameters are acquired. Alternatively, when the approach achieves the limit of iterations, store the optimal parameters r and λ , otherwise increase the value of iterations and keep looping.
- (5) Construct the NRBO-SCN model using the optimal parameters r and λ for subsequent fault type identification.

The MTF-NRBO-SCN method fault diagnosis process

In order to achieve intelligent fault detect of PMSM, a PMSM fault detect approach based on MTF-NRBO-SCN is proposed. The fault diagnosis flowchart is depicted in Fig. 5, which is divided into the following four main procedures.

- (1) Using the PMSM fault diagnosis experimental platform to collect three-phase current data under eight different operating conditions and construct the fault diagnosis sample set.
- (2) Firstly, the one-dimensional current data of each phase of the PMSM are transformed into MTF images separately. Secondly, the above three images are fused as the R, G, and B channels of the graph. Finally, the final multi-channel MTF fusion image is obtained.
- (3) The color features, shape features and texture features are excavated from the MTF fusion map to construct the PMSM multidimensional feature vector. It can effectively describe multiple attributes of the image and provide strong feature support for fault classification and recognition. Randomly divide the feature vectors into training set and testing set in the 1:1 ratio.
- (4) Firstly, the NRBO algorithm is employed to optimize the parameters of the SCN classification model and construct the optimal NRBO-SCN fault classification model. Secondly, the set of training samples is fed into the NRBO-SCN model for training to acquire the trained fault classification model. Finally, the test sample set is input into the trained fault classification model to obtain the fault identification results, and the accuracy of the fault identification model is visualized through the confusion matrix.

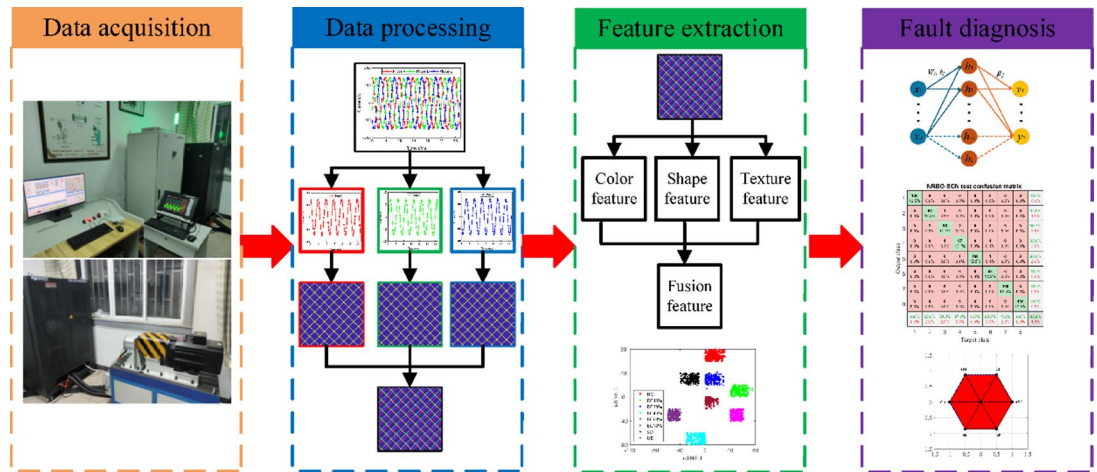


Fig. 5. The PMSM fault diagnosis flowchart based on MTF-NRBO-SCN.

Parameter	Value	Parameter	Value
Rated voltage	72 V	Stator inner diameter	108 mm
Rated power	10 Kw	Stator outer diameter	160 mm
Rated speed	3000 rpm	Rotor inner diameter	36 mm
Rated torque	19.9 N·m	Rotor outer diameter	106.66 mm
Number of pole pairs	8	Permanent magnet material	NdFeB
Number of stator slots	48	Core material	35W270

Table 2. The detailed parameters of PMSM simulation model.

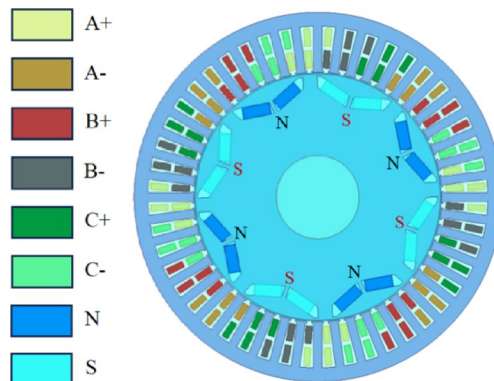


Fig. 6. The PMSM simulation model.

Proposed method validation

Validate the datasets

PMSM simulation model

To demonstrate the validity and accuracy of the MTF fusion image and NRBO-SCN fault diagnosis method, the paper simulates a 48 slot 8-pole miniature PMSM with a rated power of 10kw using Ansys Maxwell electromagnetic simulation software. The specific parameters of the PMSM simulation model are depicted in Table 2. As the laboratory already has an actual motor with this parameter, it can be used for later experimental verification. The PMSM is modeled using the main parameters in Table 2. The two-dimensional simulation model of the PMSM is depicted in Fig. 6. The detailed parameter of the PMSM simulation model is carried out with effective voltage value of 72V, rotational speed of 3000 rpm and iteration step of 0.00005s.

PMSM experimental setup

In this paper, the validity of the proposed technique is further confirmed by building a PMSM fault test platform, and the overall platform of the fault experiment is depicted in Fig. 7. The experimental platform mainly includes

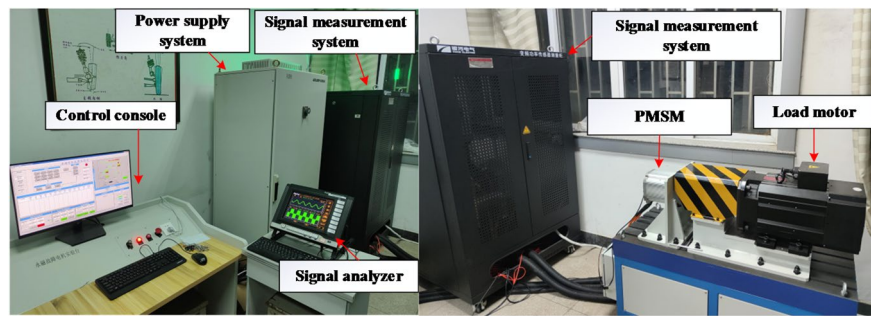


Fig. 7. The PMSM fault diagnosis experimental platform.

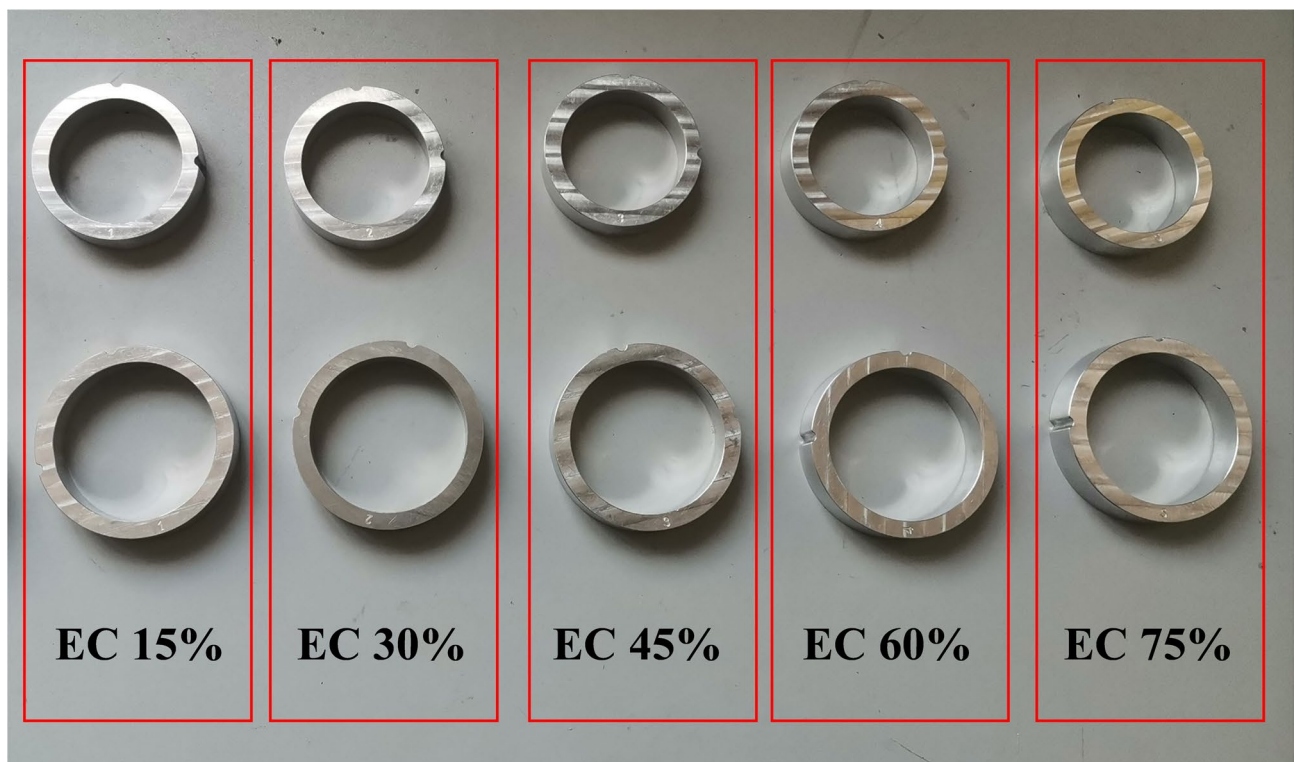


Fig. 8. Eccentric rings with different eccentricity installed on the front and back cover of PMSM.

the following parts: testing PMSM (the specific parameters is shown in Table 2), load motor, signal measurement system, signal analyzer, power supply system, and control console. The experimental conditions are set as follows: sampling frequency is 250kHz , motor speed is 3000rpm . The current sensor for collecting current signals adopts an eddy current sensor and is installed in the signal measurement system. The eccentricity (EC) fault of the motor is set by machining eccentric rings with different degrees of eccentricity. The specific eccentricity of PMSM is depicted in Fig. 8. To verify the accuracy of the PMSM simulation model, the collected experimental current signals were compared and analyzed with the simulation signals. The phase A current signal of the normal and eccentric fault 15% is displayed in Fig. 9. It can be observed that the simulated current signals of the two various states have good agreement with the current signals collected by the experimental platform, which further verifies the authenticity of the simulated current signals.

Validated by PMSM simulation model

Design the PMSM simulation datasets

Eight different operating conditions were simulated using the PMSM simulation model, and data of 1s were collected for each working condition respectively. By calculating the number of samples in one cycle is 400. To fully ensure the integrity of each set of data samples and obtain rich PMSM simulation fault datasets, the paper sets the length of each simulation data sample to 600 sampling points and uses overlapping methods to segment the data. The eight PMSM current simulation signals were labeled with sample data, and each operating condition signal contained 100 samples, for the total of 800 samples. The samples are segmented into training

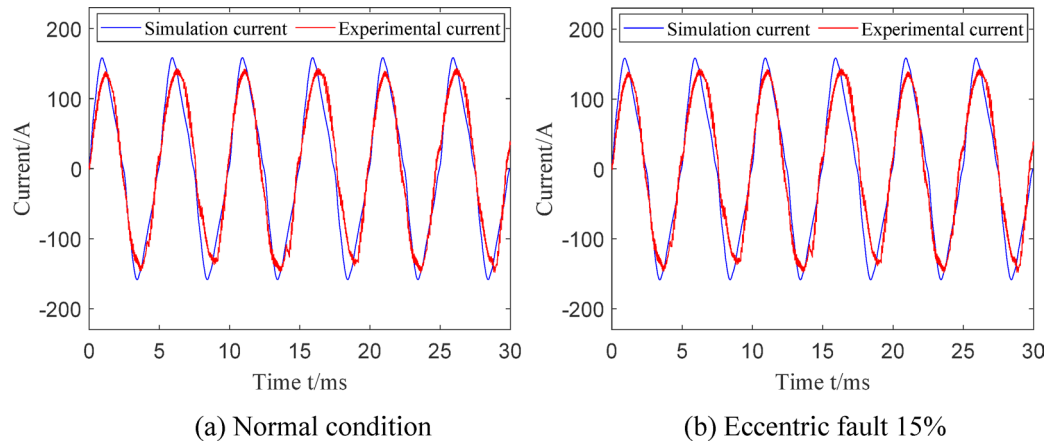


Fig. 9. The phase A current calculated by the PMSM simulation model and measured by experimental platform.

Working states	Abbreviation	Sample length	Training samples number	Testing samples number	Category label
Normal condition	NC	600	50	50	1
Eccentric fault 15%	EC15%	600	50	50	2
Eccentric fault 30%	EC30%	600	50	50	3
Eccentric fault 45%	EC45%	600	50	50	4
Eccentric fault 60%	EC60%	600	50	50	5
Eccentric fault 75%	EC75%	600	50	50	6
Single demagnetization	SD	600	50	50	7
Uniform demagnetization	UD	600	50	50	8

Table 3. The PMSM detailed simulation datasets.

set and testing set for fault identification on the basis of 1:1. The PMSM detailed simulation datasets is shown in Table 3.

The PMSM current simulation data for the first 30ms under 8 different operating conditions are depicted in Fig. 10. It can be observed that the peak three-phase current in the normal condition is minimum, and the peak three-phase current increases gradually as the the increases in the degree of eccentricity. However, the peak values of the three-phase current signals under the eight different operating conditions have a small difference and lack an obvious pattern. This makes it difficult to recognize the PMSM working conditions from the three-phase current signals. Therefore, by converting one-dimensional data into two-dimensional images, hidden fault features can be effectively extracted, aiding in subsequent fault classification and identification.

MTF two-dimensional image transformation

The one-dimensional three-phase current signal of PMSM is translated into a two-dimensional feature map with time correlation using MTF approach. The MTF image conversion and fusion flowchart is shown in Fig. 11. After converting the three-phase currents of PMSM into corresponding MTF images, which are input as the R, G, and B channels for image fusion to obtain the final MTF fusion image. Select one image for each fault sample for display, and the MTF fusion diagram of the PMSM simulation model under various working conditions is displayed in Fig. 12. From Fig. 12, it can be seen that the MTF image of the eccentric fault exhibits locally irregular speckle textures, while the MTF image of the demagnetization fault shows a global red enhancement phenomenon. The fused MTF image fully preserves the detailed features of each phase current signal, which provide a rich data information foundation for subsequent image feature extraction and fault classification recognition.

MTF fusion image feature extraction

Extract nine color features, seven shape features, and six texture features from MTF fused images under eight different operating conditions, for a total of twenty-two feature quantities. Due to the T-SNE algorithm ability to reduce high-dimensional vectors to two or three dimensions, it has a superior visualization performance and effectively preserves the original information of the data. The T-SNE approach is employed to downscale the twenty-two dimensional feature vector to a two-dimensional feature volume and visualize it. The visualization is displayed in Fig. 13. It shows that the data samples of single color feature quantity, shape feature quantity and texture feature quantity are poorly distinguishable and cannot be used for effective fault classification. In the

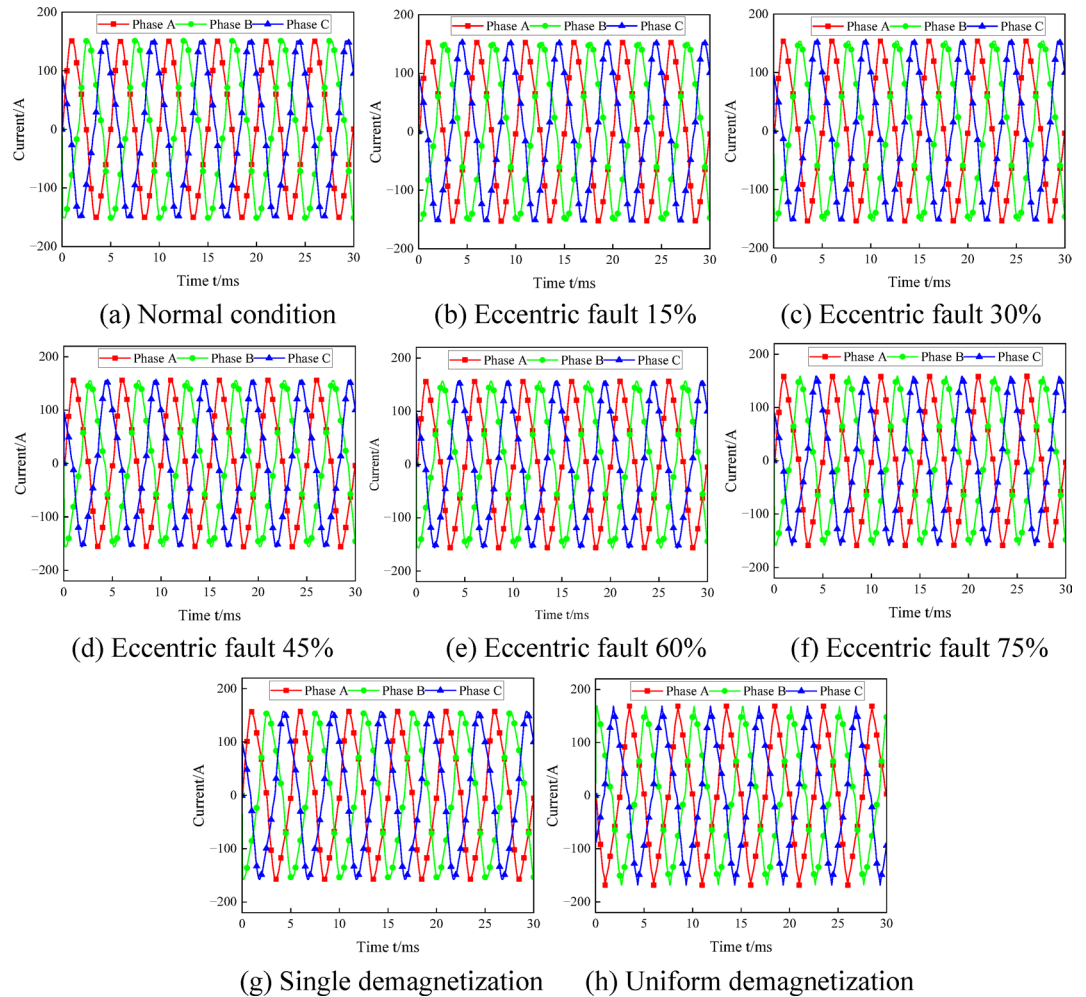


Fig. 10. Three-phase current waveform of PMSM simulation model.

two-dimensional graph that integrates feature quantities, there is no cross mixing phenomenon among samples under different operating conditions, and different types of faults can be clearly identified.

Results and discussion

Input the 22×800 dimensional fault feature vector extracted from the MTF fused image features into the NRBO-SCN model for model training to find the optimal parameters. The data sample set of the PMSM simulation model is divided into training sample set and testing sample set on 1:1 ratio. Set the parameters of the NRBO-SCN model. Maximum number of hidden layer neurons $L_{\max} = 50$, maximum number of candidate nodes $T_{\max} = 100$, and error tolerance $\varepsilon = 0.01$. The two optimized parameters λ and r are set to $[0.5, 250]$ and $[0.9, 0.999999]$. The population size of the NRBO algorithm is set to 30, and the maximum value of iterations is 100. The fitness function curve of the NRBO-SCN model on the simulation datasets is displayed in Fig. 14. As can be observed in Fig. 14, the NRBO-SCN fault classification model reaches more than 90% fault classification accuracy after the 4th iteration. When the iteration curve reaches about 40 iterations, the optimal fitness value is reached. The NRBO-SCN model can adaptively iterate to acquire the best combination parameters, which effectively improving the accuracy of fault classification.

The test sample set is fed into the trained NRBO-SCN fault model for classification and identification. The confusion matrix and classification results of the PMSM simulation datasets in the NRBO-SCN model are depicted in Fig. 15. As can be observed in Fig. 15a, most of the test sample categories were accurately categorized, with only a very small number of sample data experiencing misjudgment. In order to more clearly illustrate the types and quantities of sample misjudgments, the confusion matrix is introduced for visualization. As can be seen in Fig. 15b, only three samples-corresponding to the EC15%, EC45%, and SD categories-were misclassified. Overall, the MTF-NRBO-SCN approach achieved a fault classification accuracy of 99.2%.

To verify the advantages of the NRBO-SCN fault classification model, the paper inputs the extracted MTF fusion image feature vectors into SCN, ConvNeXt, ResNet and SVM fault classifiers for fault classification recognition. The confusion matrix and classification results are shown in Figs. 16, 17, 18 and 19. From Figs. 16, 17, 18 and 19, it can be seen that the four compared fault classification models all have a significant number of erroneous test set samples. The corresponding confusion matrices show that the classification accuracy of these

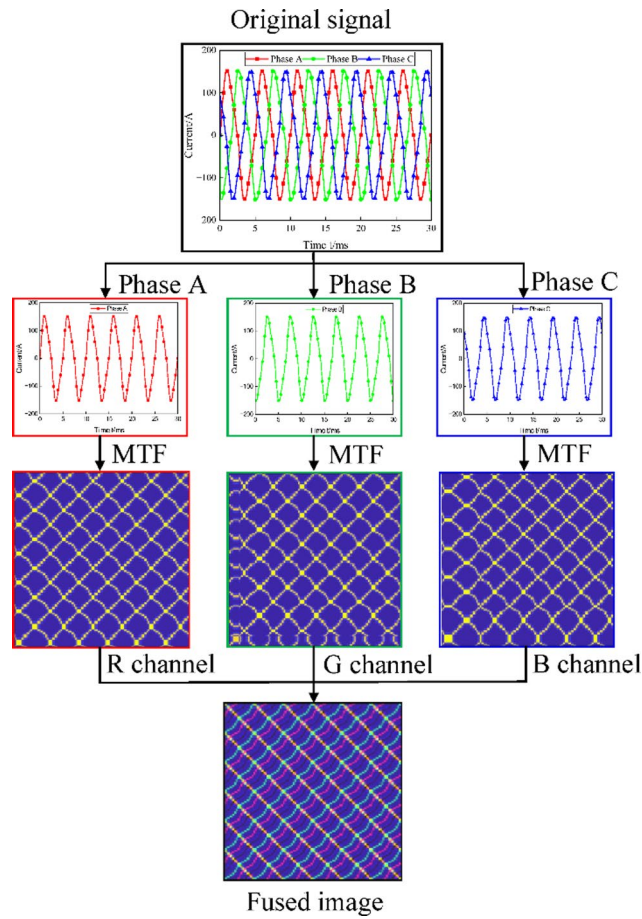


Fig. 11. MTF image conversion and fusion flowchart.

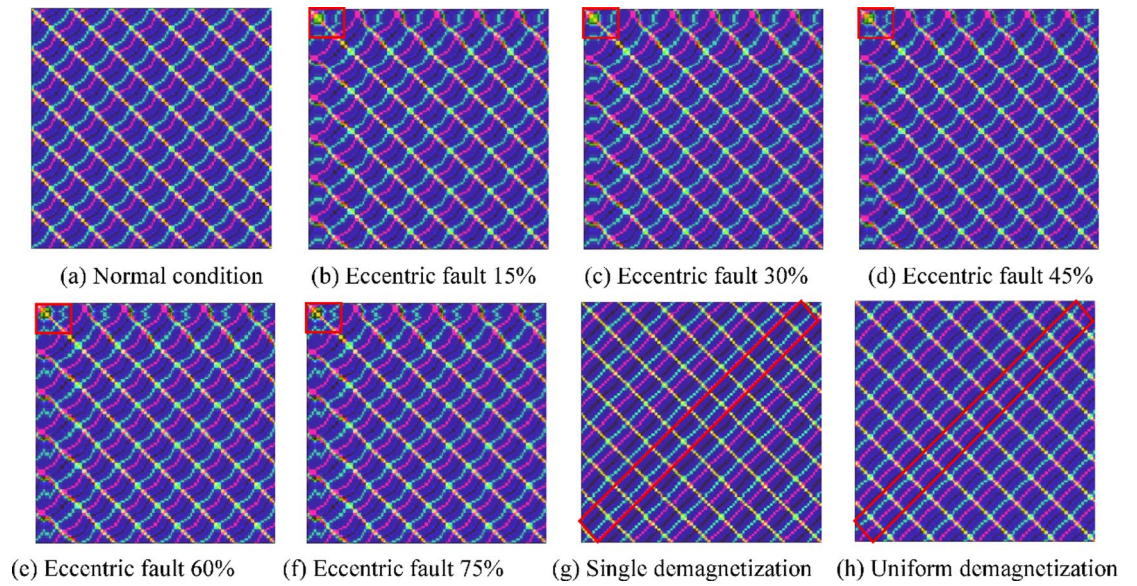


Fig. 12. The MTF fusion diagram of PMSM simulation model.

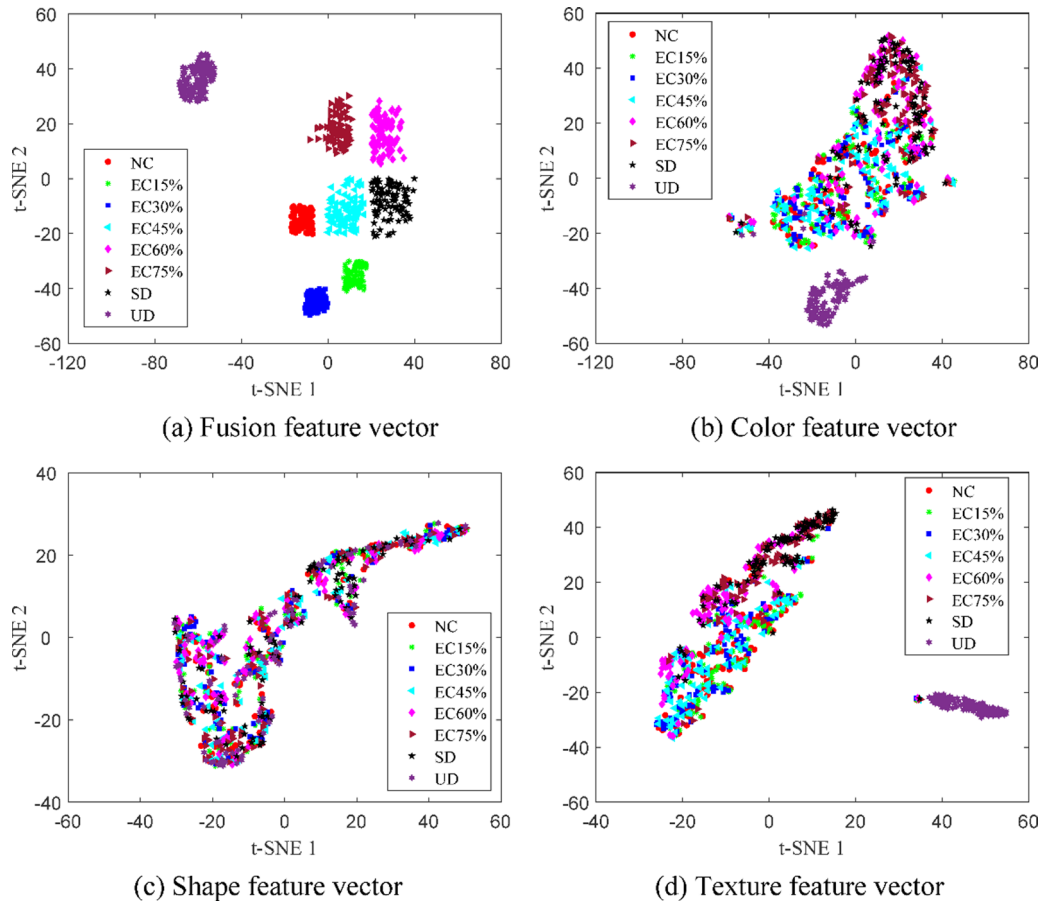


Fig. 13. Visualization of different feature vectors T-SNE.

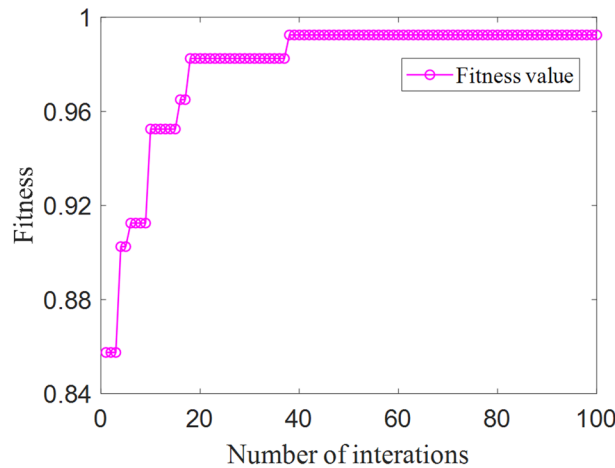


Fig. 14. The fitness function curve of NRBO-SCN model in the PMSM simulation model.

four conventional classification methods are 91.8%, 90.5%, 89.5% and 88.2%, respectively. Each of them is lower than that of the fault classification model proposed in the paper, which further verifies that NRBO-SCN has a higher classification accuracy than that of the conventional classification model.

Due to the fact that the polygon area measurement(PAM) method is a stable and efficient machine learning performance evaluation approach, the key idea of PAM approach is to evaluate the superiority or inferiority of machine learning technique by computing the polygon area between predicted labels and real labels. To further quantitatively evaluate the capability of the fault classifiers, the paper adopts the PAM method to evaluate the

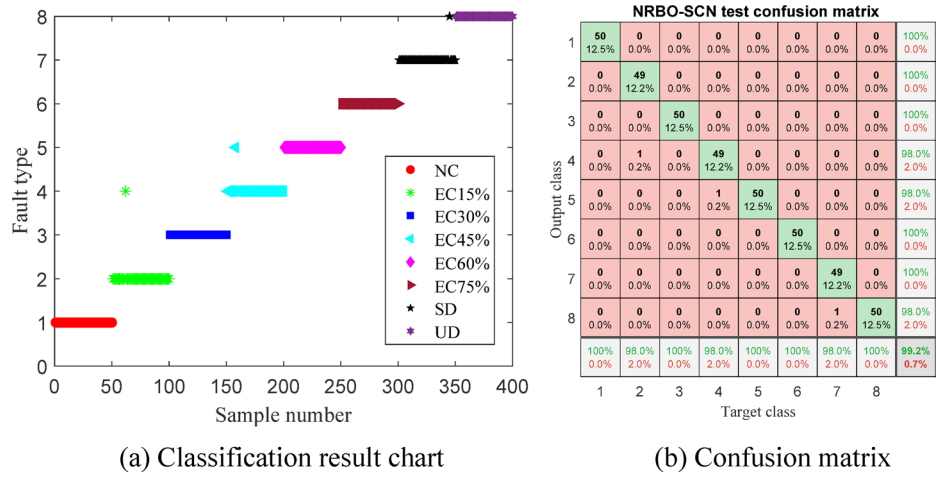


Fig. 15. The classification results of PMSM simulation datasets in the NRBO-SCN model.

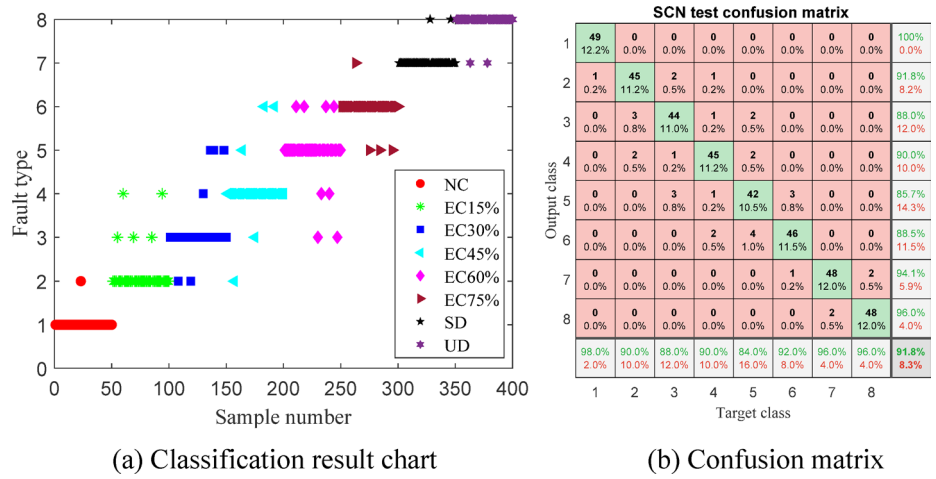


Fig. 16. The classification results of PMSM simulation datasets in the SCN model.

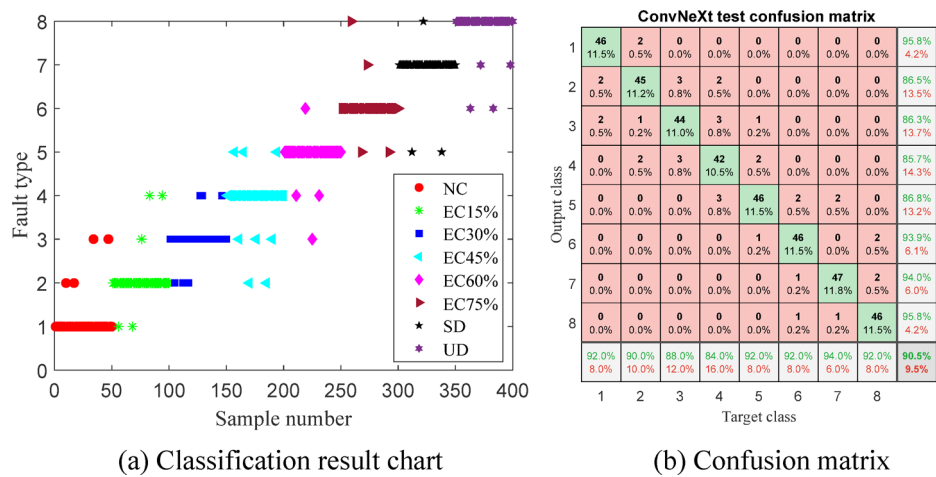


Fig. 17. The classification results of PMSM simulation datasets in the ConvNeXt model.

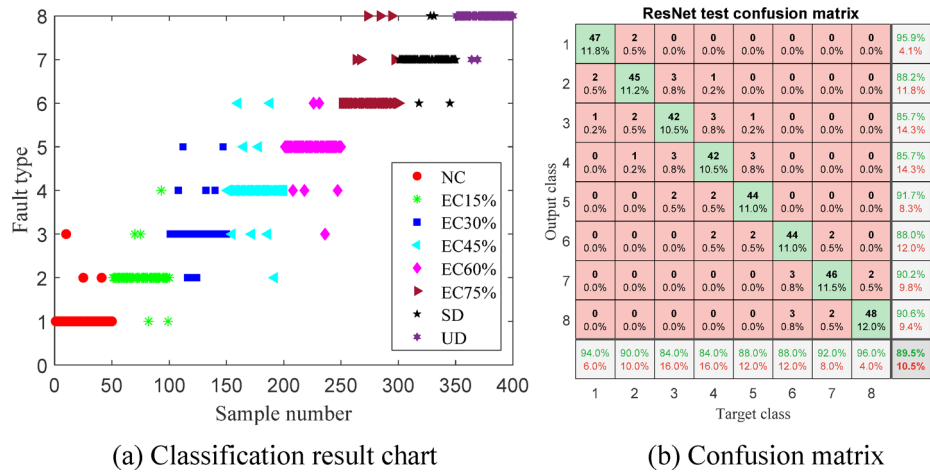


Fig. 18. The classification results of PMSM simulation datasets in the ResNet model.

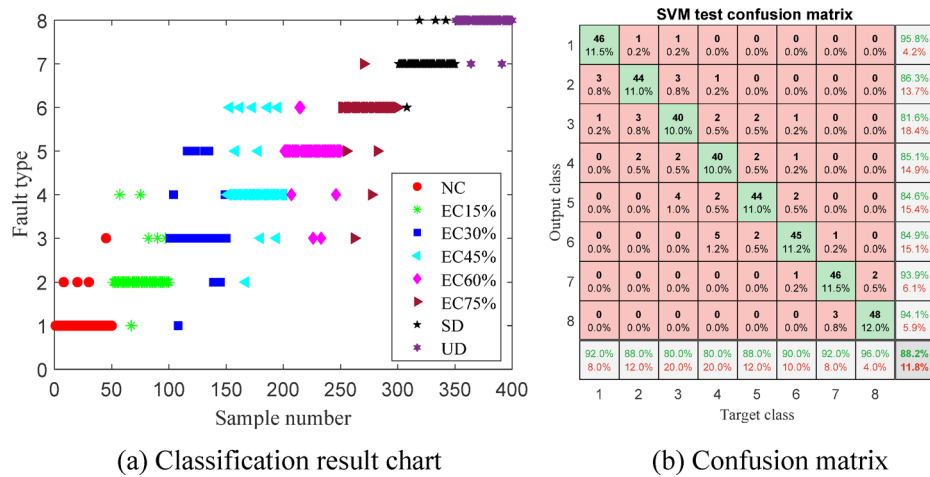


Fig. 19. The classification results of PMSM simulation datasets in the SVM model.

comprehensive performance of the five fault classifiers. The article constructs a polygon by calculating the following six evaluation indicators. The specific calculation of evaluation indicators are shown in Eqs. (47)–(52).

$$\begin{aligned}
 \text{Classification Accuracy} &= CA \\
 &= \frac{TP + TN}{TP + TN + FP + FN}
 \end{aligned}
 \tag{47}$$

$$\text{Sensitivity} = SE = \frac{TP}{TP + FN}
 \tag{48}$$

$$\text{Specificity} = SP = \frac{TN}{TN + FP}
 \tag{49}$$

$$\text{Jaccard Index} = JI = \frac{TP}{TP + FP + FN}
 \tag{50}$$

$$\text{F-measure} = FM = \frac{2TP}{2TP + FP + FN}
 \tag{51}$$

$$\text{Area Under Curve} = AUC = \int_0^1 f(x)dx
 \tag{52}$$

Where TP and TN respectively indicate the number of correctly predicted positive and negative samples. FP and FN respectively indicate the number of incorrectly predicted positive and negative samples. $f(x)$ represents the prediction score or probability of the classification model for sample x .

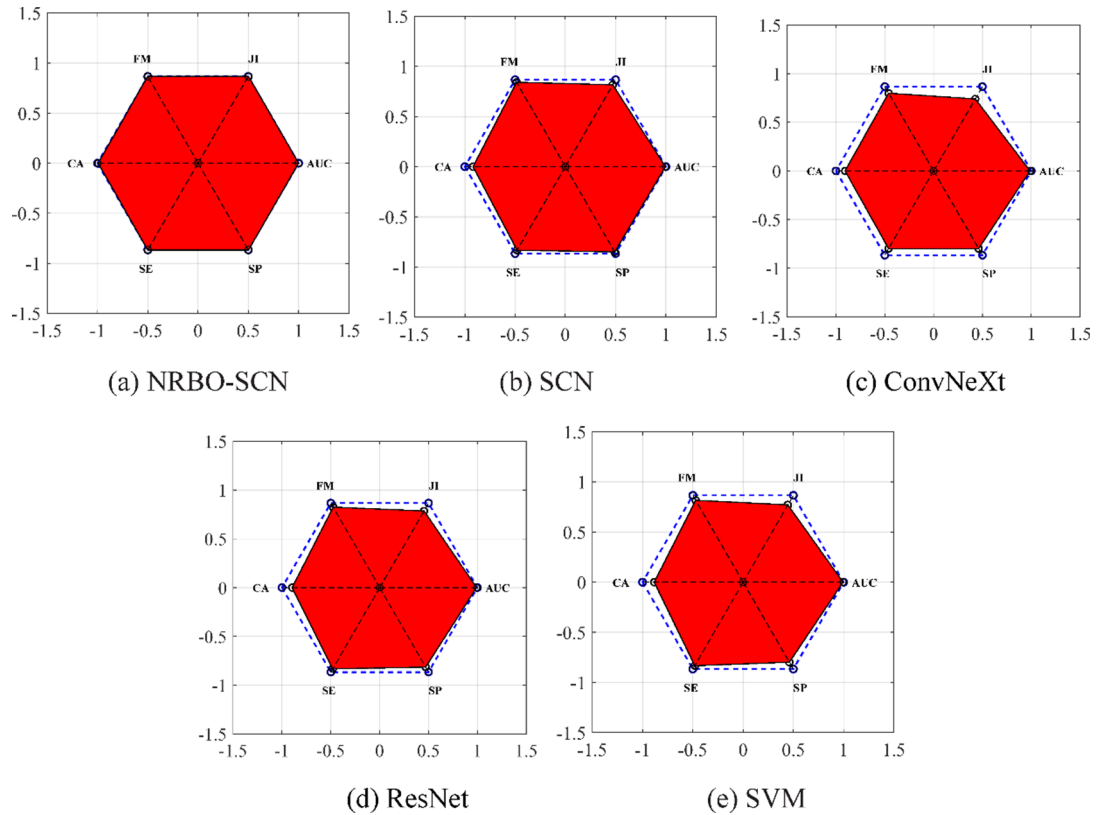


Fig. 20. The polygon area of PMSM simulation datasets.

Parameter	PAM	CA	SE	SP	AUC	JI	FM
NRBO-SCN	1	0.99	1	1	1	1	1
SCN	0.92	0.92	0.96	0.98	0.99	0.94	0.97
ConvNeXt	0.84	0.91	0.92	0.92	0.99	0.85	0.92
ResNet	0.88	0.9	0.96	0.94	0.99	0.91	0.95
SVM	0.87	0.88	0.96	0.92	0.99	0.89	0.94

Table 4. The evaluation indicators of PMSM simulation datasets in different classification methods.

By calculating the polygon area of five fault classification methods, the polygon area of the PMSM simulation datasets in different classification methods is shown in Fig. 20. The detailed calculation results of the six evaluation indicators in polygon area are shown in Table 4. Observing Fig. 20, it can be seen that the NRBO-SCN method almost completely covers the area of the hexagonal region. As can be seen in Table 4, the PAM of the NRBO-SCN method is 1, and the values of the six evaluation indicators are close to 1. However, the PAM values of the four compared methods are all less than 1, which further confirms that the classification capability of the NRBO-SCN technique is superior to the other four classification approaches.

Validity verification of three-phase fusion strategy

To evaluate the effectiveness of the proposed three-phase current MTF image fusion strategy on the PMSM simulation datasets, we selected the NC, EC45%, UD, and SD three-phase current signals from the PMSM simulation model as research subjects, and established one experimental group along with three control groups. Firstly, the experimental group synthesized MTF fusion images by converting all four signal types into MTF images and mapping them to RGB channels, whereas the three control groups were assigned to generate single-channel MTF images using only the U-phase, V-phase, or W-phase current signal, respectively. Secondly, the MTF images from the four experimental groups were used to extract 9 color features, 7 shape features, and 6 texture features, yielding a total of 22 feature vectors. Finally, the fault feature vectors were input into the NRBO-SCN fault classifier for classification. The testing accuracy of the PMSM simulation datasets under different signal sources is shown in Fig. 21, and the calculation results of fault diagnosis accuracy are shown in Table 5. It is evident from Fig. 21 that the classification accuracy achieved using the three-phase fusion MTF image was the highest, demonstrating a marked superiority over the accuracies obtained from single-phase MTF images. As shown in Table 5, the proposed three-phase fusion strategy achieves the highest classification accuracy of

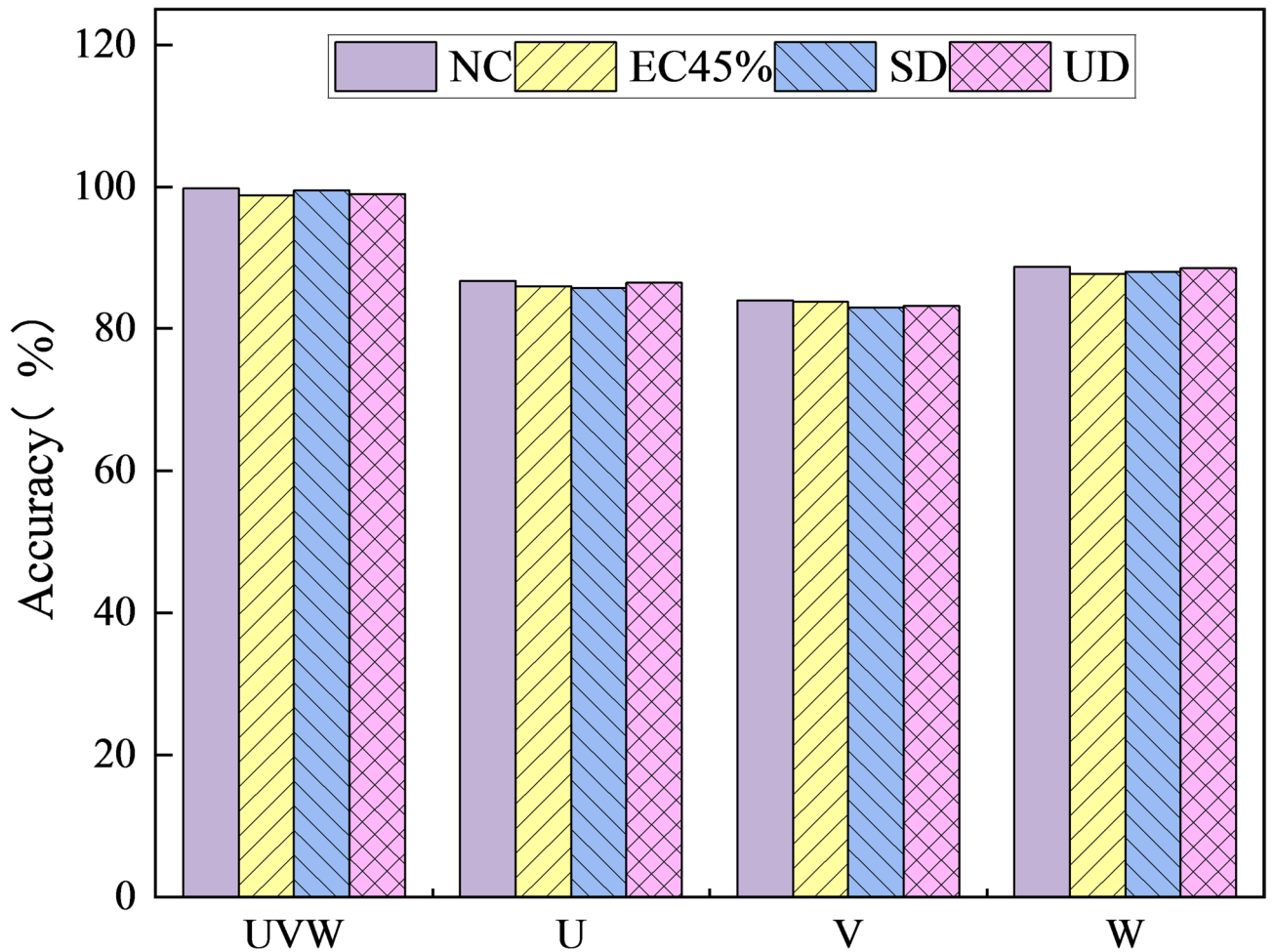


Fig. 21. The testing accuracy of the PMSM simulation datasets under different signal sources.

Signal source	NC	EC45%	SD	UD
MTF(UVW)-NRBO-SCN	99.75%	98.75%	99.5%	99%
MTF(U)-NRBO-SCN	86.75%	86%	85.75%	86.5%
MTF(V)-NRBO-SCN	84%	83.75%	83%	83.25%
MTF(W)-NRBO-SCN	88.75%	87.75%	88%	88.5%

Table 5. The fault diagnosis accuracy of the PMSM simulation datasets under different signal sources.

99.25%, with the diagnostic accuracy of all single-phase MTF images falling below 90%. The above results indicate that three-phase information fusion can provide richer fault characteristics than any single phase, effectively overcoming the defect of incomplete fault information in single-phase signals.

Analysis of noise immunity performance

To make the PMSM simulation datasets more suitable for practical application scenarios, gaussian white noise with signal-to-noise ratios(SNR) of -15dB, -5dB, 0dB, 10dB, and 35dB was added to the PMSM three-phase current simulation datasets. Simulation data containing gaussian white noise is used to convert into MTF fused image datasets, and the relevant feature vectors are extracted and fed into each fault classification model for testing respectively. The testing accuracy of each model on the PMSM simulation datasets under different noises is shown in Fig. 22, and the calculation results of fault classification accuracy is shown in Table 6. From Fig. 22, it can be seen that the classification performance of all models decreases with increasing noise intensity. From the data in Table 6, it can be observed that the accuracy of the NRBO-SCN algorithm is higher than that of the compared algorithms at different noise intensity. The calculation results demonstrate that the NRBO-SCN algorithm has high noise resistance.

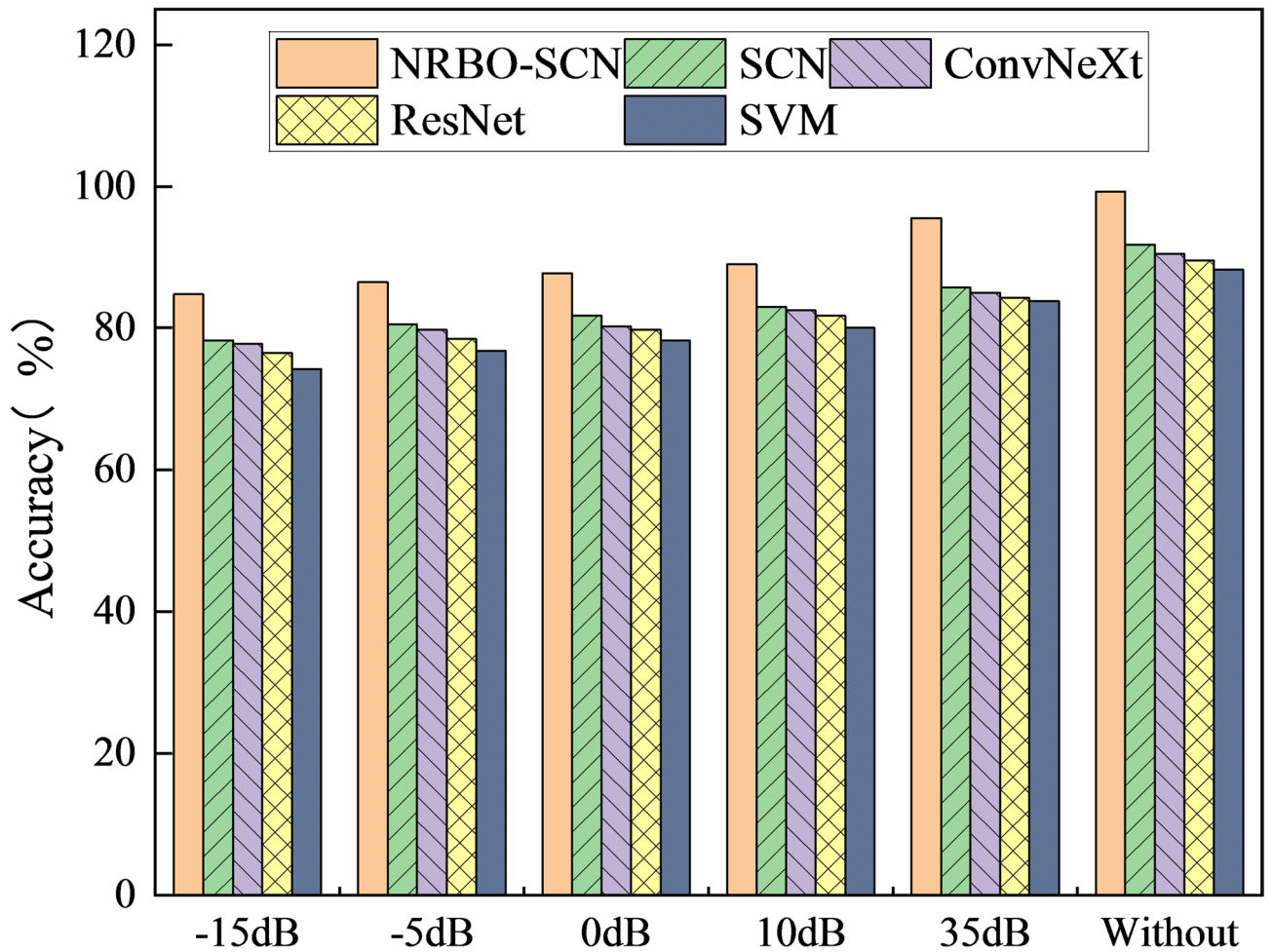


Fig. 22. The testing accuracy of various classification models on PMSM simulation datasets under different noises intensity.

Model	SNR = -15 dB	SNR = -5 dB	SNR = 0 dB	SNR = 10 dB	SNR = 35 dB	Without
NRBO-SCN	84.75%	86.5%	87.75%	89%	95.50%	99.25%
SCN	78.25%	80.5%	81.75%	83%	85.75%	91.75%
ConvNeXt	77.75%	79.75%	80.25%	82.5%	85%	90.5%
ResNet	76.5%	78.5%	79.75%	81.75%	84.25%	89.5%
SVM	74.25%	76.75%	78.25%	80%	83.75%	88.25%

Table 6. The classification accuracy of various models in PMSM simulation datasets under different noises intensity.

Validated by PMSM experimental datasets

Design the PMSM experimental datasets

The PMSM three-phase current signals were collected under eight different operating conditions, and 200 samples were collected for each operating condition, totaling 1600 samples. The data sample set is divided 1:1 into training set and testing set for later fault classification. The detailed information of the PMSM experimental datasets is shown in Table 7. The number of samples collected in one cycle is calculated to be 5000 points. To ensure the completeness of each set of data, the article sets the actual data sample length to 8000 sample points.

MTF fusion image feature extraction

In accordance with the image conversion steps of the PMSM simulation model, the process is as follows:

Firstly, convert the actual three-phase current signals of PMSM acquired through current sensor experiments into two-dimensional MTF images. Secondly, The MTF images corresponding to the three-phase current signals of PMSM are fused as input objects for the R, G, and B channels of the image to obtain the final MTF fusion

Working states	Abbreviation	Sample length	Training samples number	Testing samples number	Category label
Normal condition	NC	8000	100	100	1
Eccentric fault 15%	EC15%	8000	100	100	2
Eccentric fault 30%	EC30%	8000	100	100	3
Eccentric fault 45%	EC45%	8000	100	100	4
Eccentric fault 60%	EC60%	8000	100	100	5
Eccentric fault 75%	EC75%	8000	100	100	6
Single demagnetization	SD	8000	100	100	7
Uniform demagnetization	UD	8000	100	100	8

Table 7. The PMSM detailed experimental datasets.

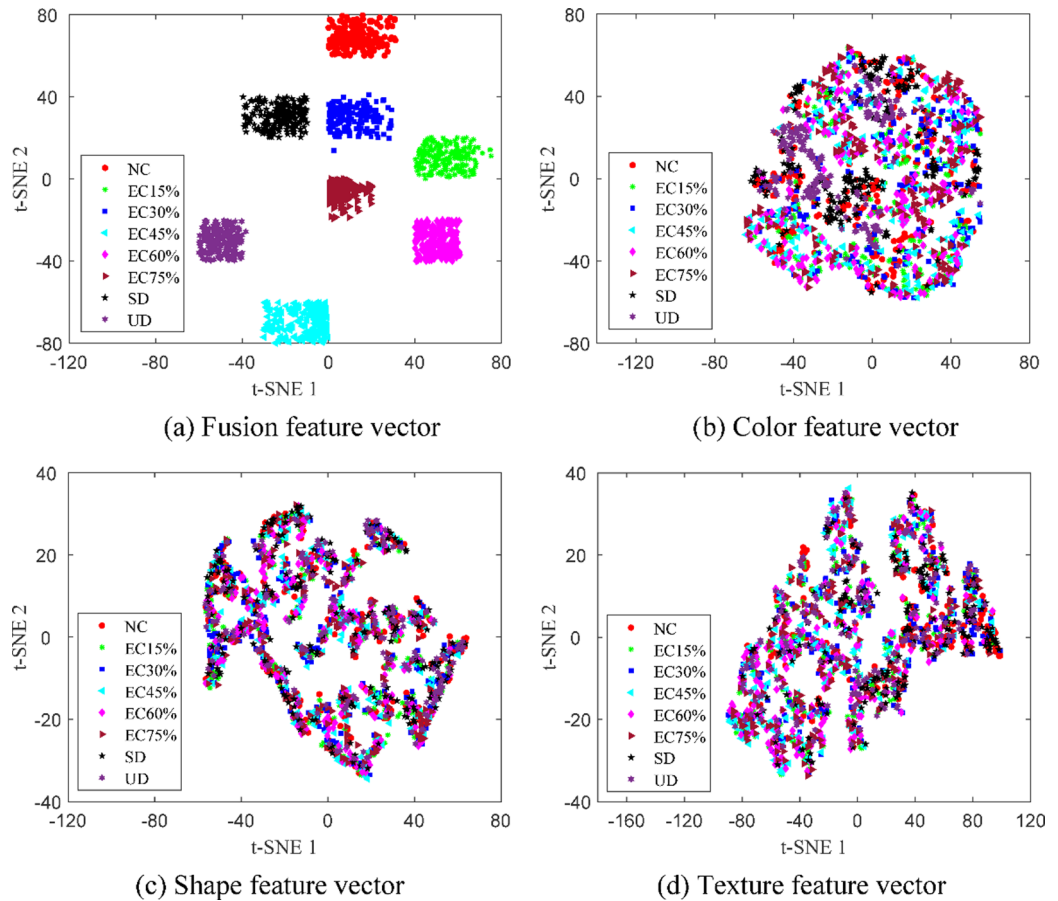


Fig. 23. Visualization of different feature vectors T-SNE.

image. Finally, extract twenty-two feature vectors, including color, shape, and texture, from the MTF fusion map of PMSM experimental data under various working states. The dimensionality reduction of the 22-dimensional feature volume using the T-SNE method can effectively enhance the distribution of different fault types and provide an intuitive visualization for fault classification. The above 22-dimensional feature vectors are reduced to two dimensional feature vectors and visualized by T-SNE method. The reduced dimension visualization graph is shown in Fig. 23. By observing in Fig. 23, it can be seen that a single feature has poor fault sample differentiation in the two dimensional graph after dimensionality reduction, and it cannot effectively differentiate between different fault types. The sample points of different working conditions in the two-dimensional graph after feature fusion dimensionality reduction are significantly separated and have good distinguish ability.

Results and discussion

The 22×1600 dimensional fault feature vectors are extracted from the MTF fused images in the experimental datasets and input to the NRBO-SCN model for training to acquire the optimal parameters. Randomly divide the fault feature vector into training set and testing set in the 1:1 ratio. The parameter settings of the NRBO-SCN model are consistent with the simulation datasets. The fitness function curve of the NRBO-SCN approach

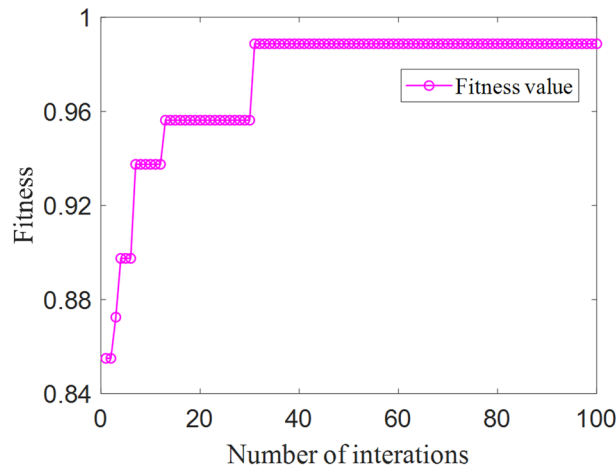


Fig. 24. The fitness function curve of NRBO-SCN model in the PMSM experimental datasets.

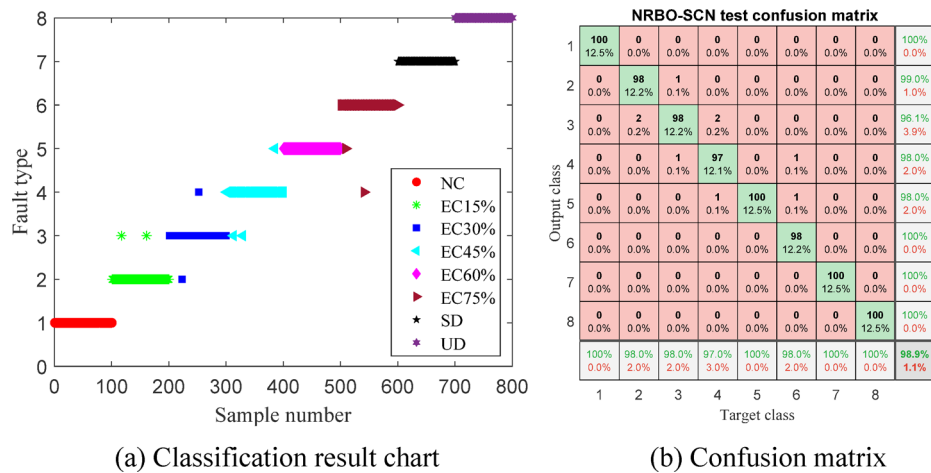


Fig. 25. The classification results of PMSM experimental datasets in the NRBO-SCN model.

on the experimental datasets is displayed in Fig. 24. From Fig. 24, it can be observed that the classification model converges when the iteration curve reaches about thirty iterations. It demonstrates that the NRBO-SCN approach has strong feature learning capability and classification performance.

The set of 800 testing samples was fed into the trained NRBO-SCN approach for classification and recognition. The confusion matrix and classification results of the PMSM experimental datasets in the NRBO-SCN model are shown in Fig. 25. From Fig. 25a, it can be seen that the NRBO-SCN model achieves accurate discrimination for the vast majority of samples, and only a small number of data samples have classification bias. From Fig. 25b, it can be seen that only nine samples were misclassified in the EC15%, EC30%, EC45%, and EC75% data samples. It indicates that the overall classification accuracy is 98.9%.

To compare the classification performance of NRBO-SCN with SCN, ConvNeXt, ResNet, and SVM models, the paper inputs the MTF fusion feature vectors into four types of fault classifiers for classification and recognition. The classification results and confusion matrix are depicted in Figs. 26, 27, 28 and 29.

From Figs. 26, 27, 28 and 29, it can be observed that compared with the NRBO-SCN approach, the four compared fault classification methods have many incorrect classification samples in the PMSM experimental data samples. The confusion matrix of the comparison model shows corresponding accuracy of 90.6%, 88.9%, 87.9%, and 86.6%. The identification accuracy of the four models is obviously lower than that of the NRBO-SCN approach presented in the paper.

To further evaluate the performance of these five fault classification methods comprehensively, six dimensional evaluation index was used to construct a polygon, and the covered polygon area was calculated for quantitative comparison. The polygon area of the PMSM experimental datasets in different classification methods is shown in Fig. 30. To quantify the differences in classification capability among different technique, the detailed calculation results of the six evaluation indicators in polygon area is shown in Table 8. From Fig. 30, it can be observed that the hexagonal area of the NRBO-SCN method is the closest to the theoretical maximum, and the remaining four classification methods have some gap with the theoretical maximum. From the data

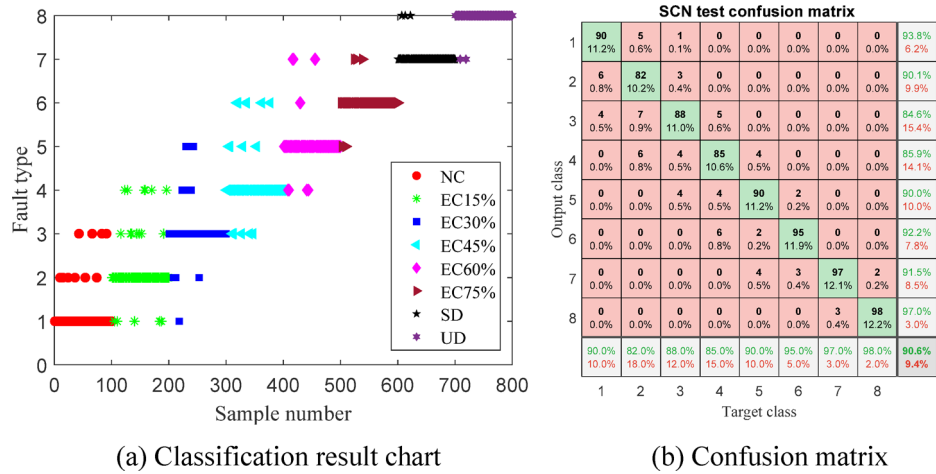


Fig. 26. The classification results of PSM experimental datasets in the SCN model.

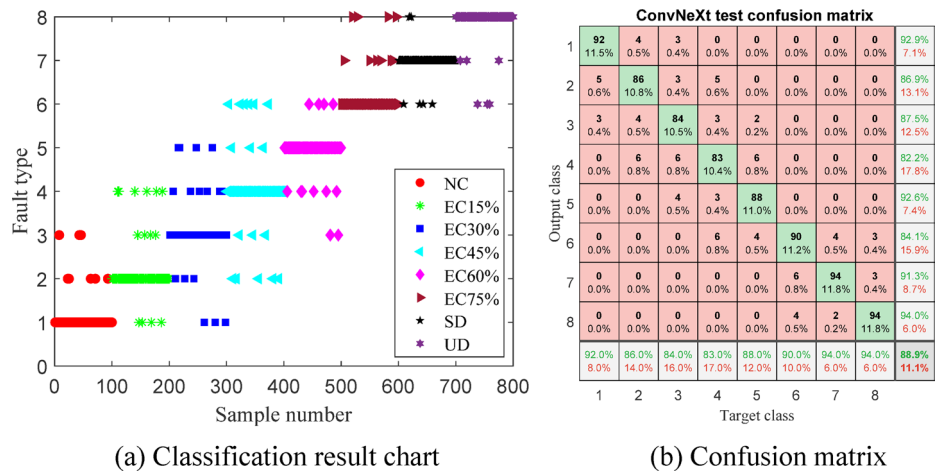


Fig. 27. The classification results of PSM experimental datasets in the ConvNeXt model.

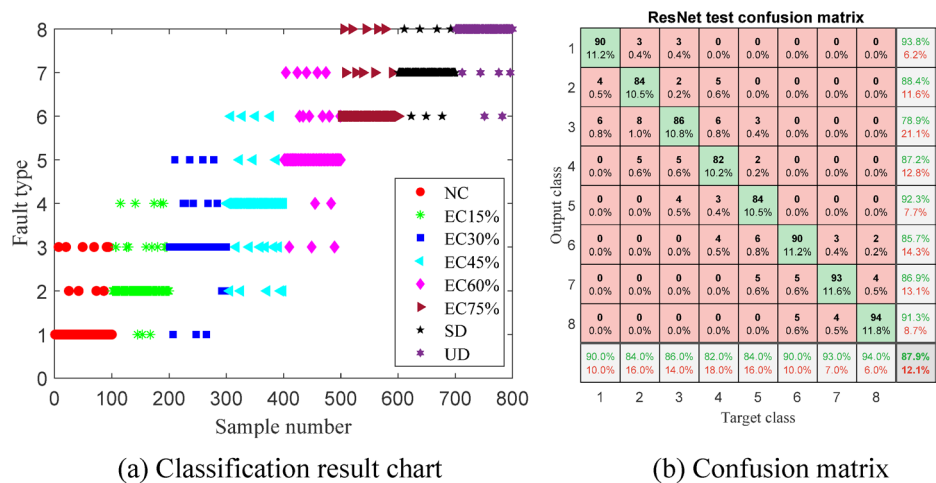


Fig. 28. The classification results of PSM experimental datasets in the ResNet model.

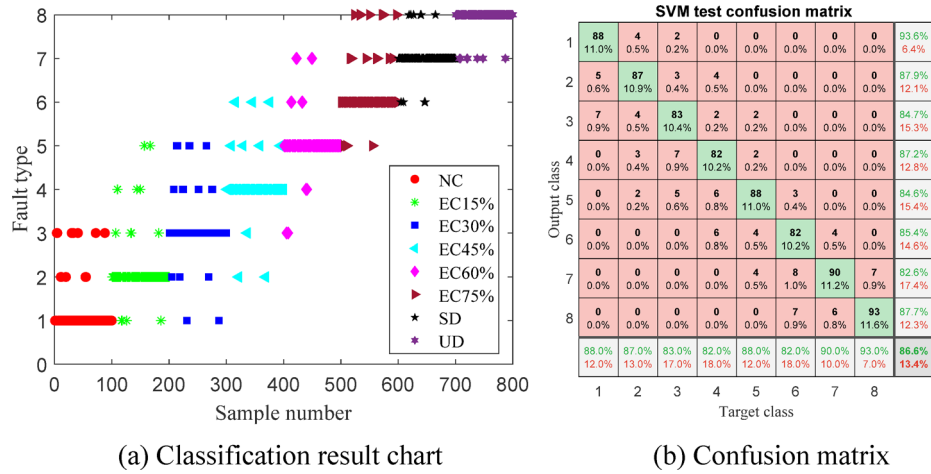


Fig. 29. The classification results of PMSM experimental datasets in the SVM model.

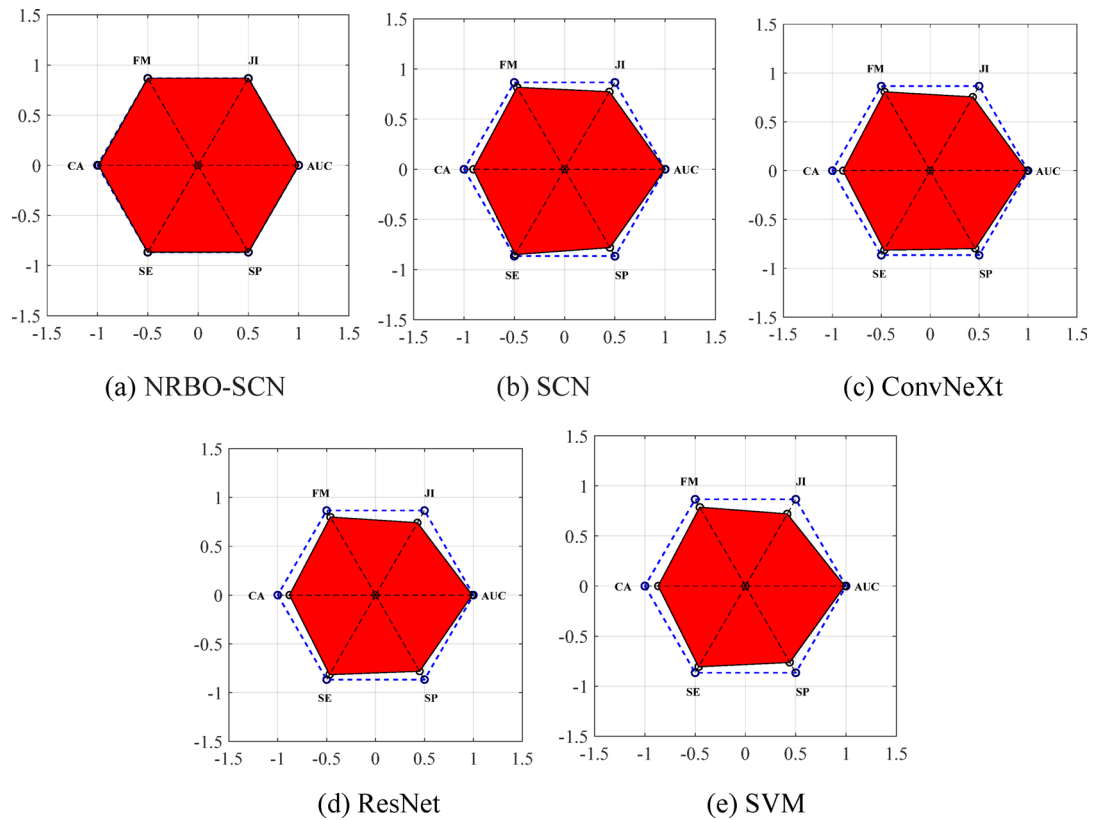


Fig. 30. The polygon area of PMSM experimental datasets.

in Table 8, it can be clearly seen that all six evaluation indicators of the NRBO-SCN method are close to 1, while the PAM values of the other four comparison methods are significantly lower than 1. It further confirms that the proposed NRBO-SCN method has superior classification performance.

Validity verification of three-phase fusion strategy

To further evaluate the three-phase current fusion strategy in real industrial environments, this study selected PMSM three-phase current signals under NC, EC45%, UD, and SD conditions as research subjects. Firstly, for the experimental group, the three-phase current signal was converted into three separate MTF images, which were then assigned to the RGB channels, respectively, to form a single fused image. The three control groups, in contrast, generated single-channel MTF images using only the U-phase, V-phase, or W-phase current signals. Secondly, the color, shape, and texture feature vectors were extracted from all generated MTF images and

Parameter	PAM	CA	SE	SP	AUC	Jl	FM
NRBO-SCN	1	0.99	1	1	1	1	1
SCN	0.87	0.91	0.98	0.9	1	0.89	0.94
ConvNeXt	0.85	0.89	0.94	0.92	0.99	0.87	0.93
ResNet	0.83	0.88	0.94	0.90	0.99	0.85	0.92
SVM	0.81	0.87	0.93	0.88	0.98	0.83	0.91

Table 8. The evaluation indicators of PMSM experimental datasets in different classification methods.

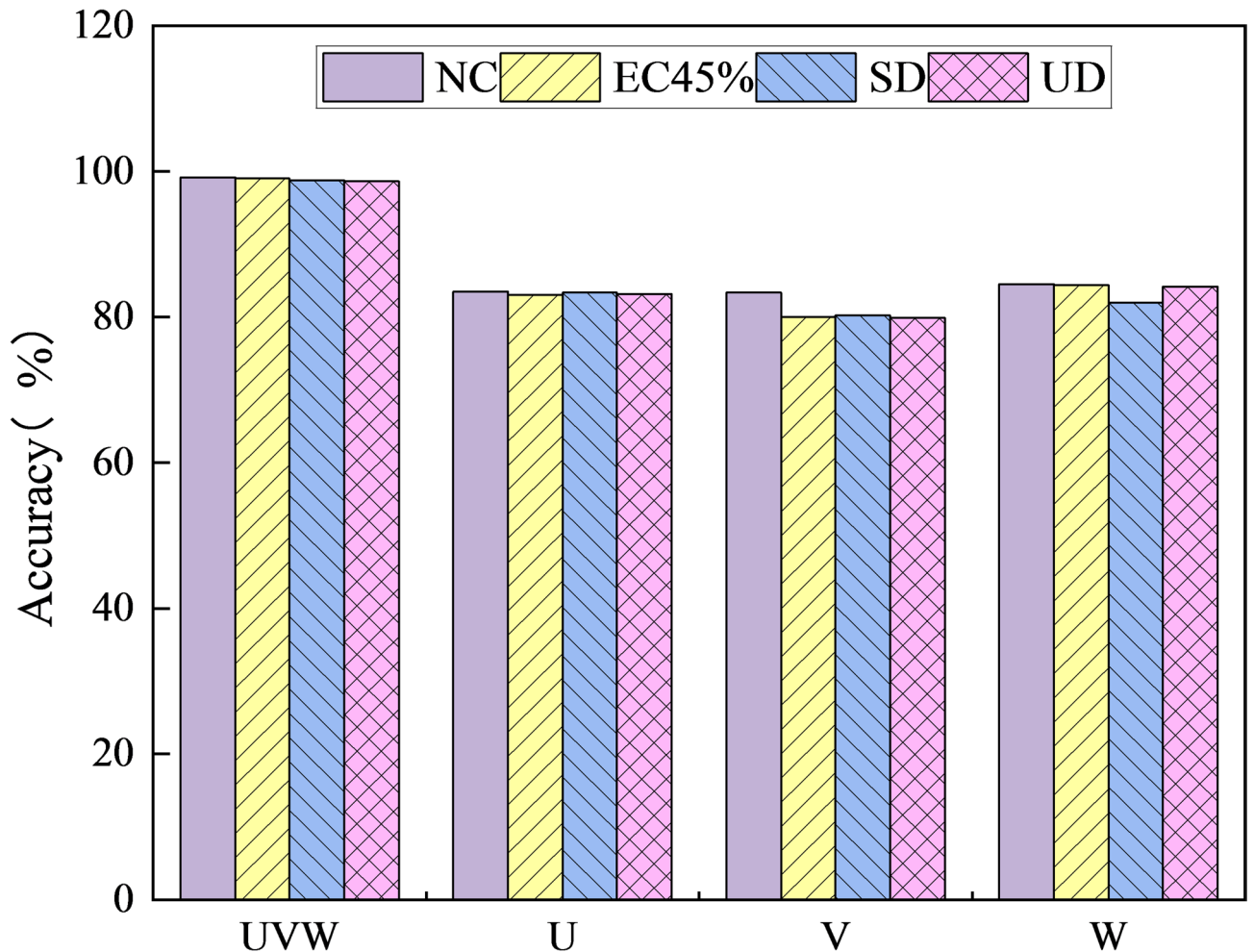


Fig. 31. The testing accuracy of the PMSM experimental datasets under different signal sources.

combined to form a 22-dimensional fault feature vectors. Finally, the constructed feature vectors were divided into training and testing sets using 1:1 ratio and was fed into the NRBO-SCN model for training and evaluation. The testing accuracy of the PMSM experimental datasets under different signal sources is shown in Fig. 31, and the calculation result of fault diagnosis accuracy is shown in Table 9. From Fig. 31, it can be seen that the fault accuracy of the single-phase MTF images is significantly lower than that of the three-phase fused MTF images. As shown in Table 9, the three-phase fusion strategy also demonstrated high diagnostic accuracy on the experimental PMSM datasets, achieving an average of 98.87%, which is significantly higher than the best single-phase scheme (W-phase, 84.25%). These results demonstrate that the proposed three-phase fusion strategy significantly enhances fault diagnosis accuracy by mitigating the loss of fault information inherent in single-phase signals.

Analysis of noise immunity performance

To enhance the engineering applicability of the presented fault diagnosis approach, gaussian white noise with SNR of -15dB, -5dB, 0dB, 10dB, and 35dB was added to the three-phase current data of PMSM experiments to accurately simulate the real working environment of PMSM. The experimental data containing different noises

Signal source	NC	EC45%	SD	UD
MTF(UVW)-NRBO-SCN	99.13%	99%	98.75%	98.63%
MTF(U)-NRBO-SCN	83.5%	83%	83.38%	83.13%
MTF(V)-NRBO-SCN	83.38%	80%	80.25%	79.88%
MTF(W)-NRBO-SCN	84.5%	84.38%	82%	84.13%

Table 9. The fault diagnosis accuracy of the PMSM experimental datasets under different signal sources.

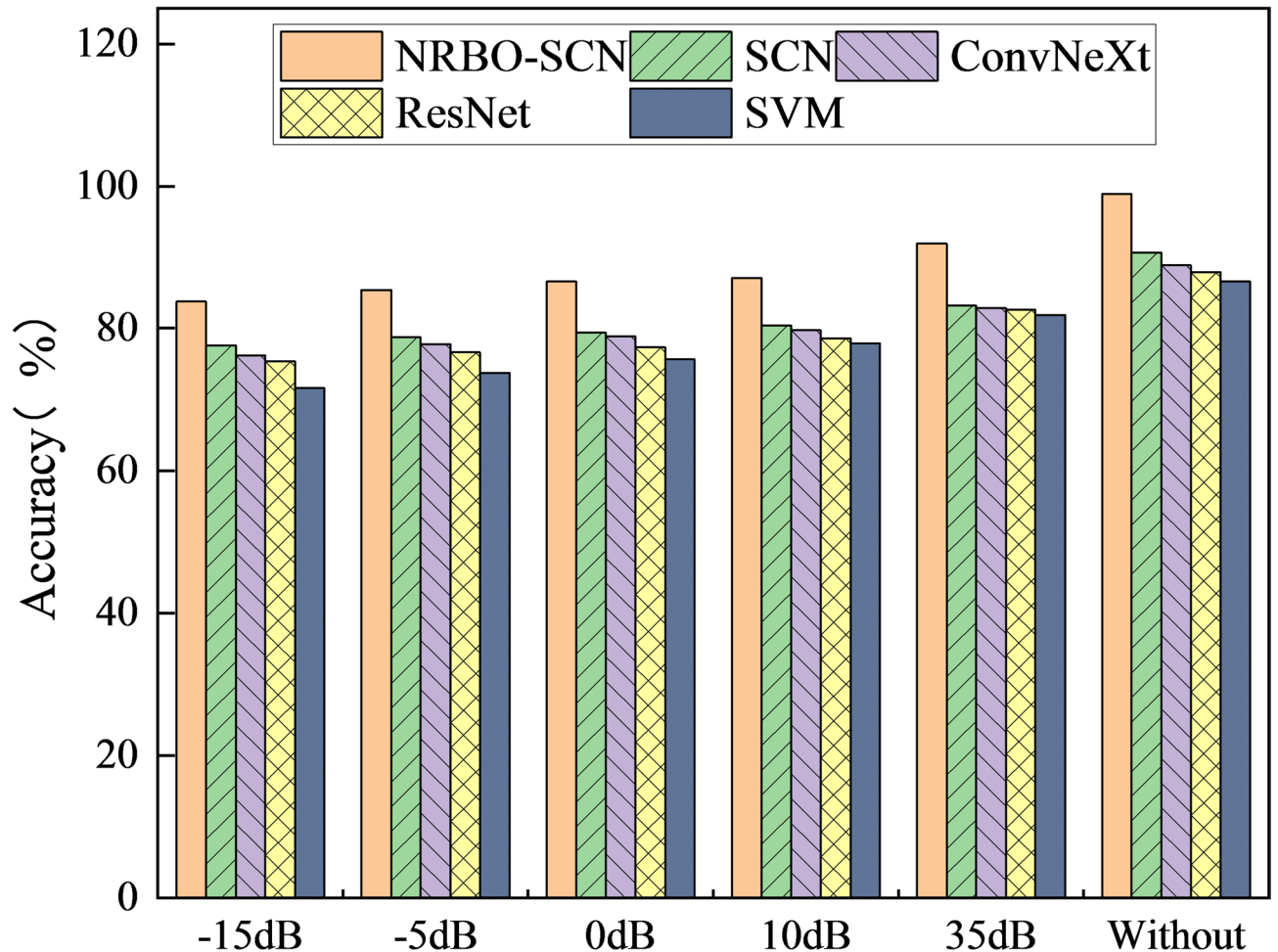


Fig. 32. The testing accuracy of different classification models on PMSM experimental datasets under different noise intensities.

are converted into MTF fused images and the image feature vectors are extracted and inputted into different fault classifiers for identification and classification. The testing accuracy of each model on the PMSM experimental datasets under different level of noises is displayed in Fig. 32. The calculation results of fault classification accuracy is shown in Table 10. From Fig. 32, it can be observed that the noise environment has a remarkable effect on the classification accuracy of the fault classification model. As shown in Table 10, the NRBO-SCN model maintains the highest classification accuracy across all five noise types, demonstrating significant noise robustness.

Conclusions

- (1) From the perspective of data enhancement, MTF coding is applied to transform the three-phase current signal into the two-dimensional image, which effectively enhances the fault characteristic information. To comprehensively enhance the feature saliency of images, the three-phase MTF images were fused with RGB channels, which improved the quality of sample training.

Model	SNR = -15 dB	SNR = -5 dB	SNR = 0 dB	SNR = 10 dB	SNR = 35 dB	Without
NRBO-SCN	83.75%	85.38%	86.63%	87.13%	91.88%	98.88%
SCN	77.63%	78.75%	79.38%	80.38%	83.25%	90.63%
ConvNeXt	76.25%	77.75%	78.88%	79.75%	82.88%	88.88%
ResNet	75.38%	76.63%	77.38%	78.63%	82.63%	87.88%
SVM	71.63%	73.75%	75.63%	77.88%	81.88%	86.63%

Table 10. The classification accuracy of various models in PMSM experimental datasets under different noises intensity.

- (2) Extracting color, shape, and texture feature vectors from MTF fused images can captures comprehensive fault feature information from multiple angles and levels. It effectively avoids the issue of missing fault feature information caused by single feature.
- (3) The NRBO algorithm is employed to optimize the parameters of the SCN classification model, significantly enhancing its ability to adaptively adjust model parameters. By using PMSM simulation and experimental datasets for verification, the NRBO-SCN method has superior fault identification ability and strong noise resistance performance compared with conventional fault classification methods.

Data availability

The datasets used during the current study are available from the corresponding author upon reasonable request.

Received: 1 October 2025; Accepted: 21 November 2025

Published online: 27 November 2025

References

1. Zhan, L., Xu, X., Qiao, X., Qian, F. & Luo, Q. Fault feature extraction method of a permanent magnet synchronous motor based on VAE-WGAN. *Processes* **10**(2), 200. <https://doi.org/10.3390/pr10020200> (2022).
2. Huang, F. et al. Demagnetization fault diagnosis of permanent magnet synchronous motors using magnetic leakage signals. *IEEE T Ind. Inf.* **19**(4), 6105–6116. <https://doi.org/10.1109/TII.2022.3165283> (2023).
3. Feng, L., Luo, H., Xu, S. & Du, K. Inverter fault diagnosis for a three-phase permanent magnet synchronous motor drive system based on SDAE-GAN-LSTM. *Electronics*. **12**(19), 4172. <https://doi.org/10.3390/electronics12194172> (2023).
4. Fan, H. et al. Intelligent fault diagnosis of rolling bearing using FCM clustering of EMD-PWVD vibration images. *IEEE Access*. **8**, 145194–145206. <https://doi.org/10.1109/ACCESS.2020.3012559> (2020).
5. Pietrzak, M. Demagnetization fault diagnosis of permanent magnet synchronous motors based on stator current signal processing and machine learning algorithms. *Sensors* **23**(4), 1757. <https://doi.org/10.3390/s23041757> (2023).
6. Halder, S., Bhat, S. & Dora, B. Start-up transient analysis using CWT and ridges for broken rotor bar fault diagnosis. *Electr. Eng.* **105**(1), 221–232. <https://doi.org/10.1007/s00202-022-01657-7> (2023).
7. El-Dalahmeh, M., Al-Greer, M., Bashir, I., Demirel, A. & Keysan, O. Autonomous fault detection and diagnosis for permanent magnet synchronous motors using combined variational mode decomposition, the Hilbert-Huang transform, and a convolutional neural network. *Comput. Electr. Eng.* **100**, 108894. <https://doi.org/10.1016/j.compeleceng.2023.108894> (2023).
8. Zhang, Q., Cui, J., Xiao, W., Mei, L. & Yu, X. Demagnetization fault diagnosis of a PMSM for electric drilling tools using GAF and CNN. *Electronics* **13**(1), 189. <https://doi.org/10.3390/electronics13010189> (2024).
9. Yuan, H. et al. Fault diagnosis of bearing in PMSM based on calibrated stator current residual signal and improved symmetrized Dot pattern. *IEEE Sens. J.* **24**(3), 3232–3246. <https://doi.org/10.1109/JSEN.2023.3340408> (2024).
10. Jiang, Y. & Xie, J. VMD-RP-CSRNN based fault diagnosis method for rolling bearings. *Electronics* **11**(23), 4046. <https://doi.org/10.3390/electronics11234046> (2022).
11. Lei, C. et al. Rolling bearing fault diagnosis method based on MTF and PC-MDCNN. *J. Mech. Sci. Technol.* **38**(7), 3315–3325. <https://doi.org/10.1007/s12206-024-0606-y> (2024).
12. Mohammadi, F. & Saif, M. A multi-stage hybrid open-circuit fault diagnosis approach for three-phase VSI-Fed PMSM drive systems. *IEEE Access*. **11**, 137328–137342. <https://doi.org/10.1109/ACCESS.2023.3339549> (2023).
13. Shih, K., Hsieh, M., Chen, B. & Huang, S. Machine learning for inter-turn short-circuit fault diagnosis in permanent magnet synchronous motors. *IEEE T Magn.* **58**(8), 8204307. <https://doi.org/10.1109/TMAG.2022.3169173> (2022).
14. Song, J., Nie, X., Wu, C. & Zheng, N. A novel intelligent fault diagnosis method of rolling bearings based on the ConvNeXt network with improved denseblock. *Sensors* **24**(24), 7909. <https://doi.org/10.3390/s24247909> (2024).
15. Li, X. et al. Fusion innovation: Multi-scale dilated collaborative model of ConvNeXt and MSDA for fault diagnosis. *Robot Auton. Syst.* **182**, 104819. <https://doi.org/10.1016/j.robot.2024.104819> (2024).
16. Shen, K. & Zhao, D. Fault analysis and fault degree evaluation via an improved ResNet method for aircraft hydraulic system. *Sci. Rep.* **15**(1), 4132. <https://doi.org/10.1038/s41598-025-86634-3> (2025).
17. Zhang, X., Pan, X., Zeng, H. & Zhou, H. Intelligent diagnosis method for typical co-frequency vibration faults of rotating machinery based on Sae and ensemble resnet-svm. *Chin. J. Mech. Eng-en.* **37**(1), 64. <https://doi.org/10.1186/s10033-024-01046-0> (2024).
18. Lei, X., Lu, N., Chen, C. & Wang, C. An AVMD-DBN-ELM model for bearing fault diagnosis. *Sensors* **22**(23), 9396. <https://doi.org/10.3390/s22239369> (2022).
19. Liu, F. et al. Fault diagnosis of rolling bearing combining improved AWSGMD-CP and ACO-ELM model. *Measurement* **209**, 112531. <https://doi.org/10.1016/j.measurement.2023.112531> (2023).
20. Wu, Y., Zhang, Z., Li, Y. & Sun, Q. Open-circuit fault diagnosis of six-phase permanent magnet synchronous motor drive system based on empirical mode decomposition energy entropy. *IEEE Access*. **9**, 91137–91147. <https://doi.org/10.1109/ACCESS.2021.3090814> (2021).
21. Xing, Z., Liu, Y., Wang, Q. & Fu, J. Fault diagnosis of rotating parts integrating transfer learning and ConvNeXt model. *Sci. Rep.* **15**(1), 190. <https://doi.org/10.1038/s41598-024-84783-5> (2025).
22. Wei, D., Liu, K., Wang, J., Zhou, S. & Li ResNet-18-based interturn short-circuit fault diagnosis of PMSMs with consideration of speed and current loop bandwidths. *IEEE T Transa Electr.* **10**(3), 5805–5818. <https://doi.org/10.1109/TTE.2023.3319157> (2023).
23. Xu, F., Liu, Y. & Wang, L. An improved ELM-WOA based fault diagnosis for electric power. *Front. Energy Res.* **11**, 1135741. <https://doi.org/10.3389/fenrg.2023.1135741> (2023).

24. Wang, D. & Li, M. Stochastic configuration networks: fundamentals and algorithms. *IEEE T Cybernetics*. **47**(10), 3466–3479. <https://doi.org/10.1109/TCYB.2017.2734043> (2017).
25. Ji, H., Huang, K. & Mo, C. Research on the application of variational mode decomposition optimized by snake optimization algorithm in rolling bearing fault diagnosis. *Shock Vib*. **2024**, 5549976. <https://doi.org/10.1155/2024/5549976> (2024).
26. Li, G. et al. SO-IMCKD processed signal improving MSCNN models fault diagnosis accuracy for drilling pump fluid end. *Meas. Sci. Technol*. **34**(11), 115115. <https://doi.org/10.1088/1361-6501/ace8ae> (2023).
27. Yan, P. et al. Transformer fault diagnosis based on DBO-BiLSTM algorithm and LIF technology. *Meas. Sci. Technol*. **35**(11), 115202. <https://doi.org/10.1088/1361-6501/ad6686> (2024).
28. Zhang, D., Zhang, C., Han, X. & Wang, C. Improved DBO-VMD and optimized DBN-ELM based fault diagnosis for control valve. *Meas. Sci. Technol*. **35**(7), 075103. <https://doi.org/10.1088/1361-6501/ad3be0> (2024).
29. Wang, Q., Hu, S. & Wang, X. Detection of incipient rotor unbalance fault based on the RIME-VMD and modified-WKN. *Sci. Rep*. **14**(1), 4683. <https://doi.org/10.1038/s41598-024-54984-z> (2024).
30. Su, H. et al. RIME: A physics-based optimization. *Neurocomputing* **532**, 183–214. <https://doi.org/10.1016/j.neucom.2023.02.010> (2023).
31. Abdel-Basset, M., Mohamed, R. & Abouhawwash, M. Crested Porcupine optimizer: A new nature-inspired metaheuristic. *Knowl-Based Syst*. **284**, 111257. <https://doi.org/10.1016/j.knsys.2023.111257> (2024).
32. Liu, S., Jin, Z., Lin, H. & Lu, H. An improve crested Porcupine algorithm for UAV delivery path planning in challenging environments. *Sci. Rep*. **14**(1), 20445. <https://doi.org/10.1038/s41598-024-71485-1> (2024).
33. Sowmya, R., Premkumar, M. & Jangir, P. Newton-Raphson-based optimizer: A new population-based metaheuristic algorithm for continuous optimization problems. *Eng. Appl. Artif. Intel*. **128**, 107532. <https://doi.org/10.1016/j.engappai.2023.107532> (2024).
34. Abdel-Basset, M., Mohamed, R., Hezam, I., Sallam, K. & Hameed, I. Parameters identification of photovoltaic models using Lambert W-function and Newton-Raphson method collaborated with AI-based optimization techniques: A comparative study. *Expert Syst. Appl*. **225**, 12477. <https://doi.org/10.1016/j.eswa.2024.124777> (2024).

Author contributions

H.G. wrote the main manuscript text, Y.Y. contributed to the conception and design of the work, G.C. reviewed paper and gave the comments, D.Z. proposed original research idea and provide research funding, Y.H. reviewed and revised the article, and J.Y. provided guidance on the theoretical section. All authors read and approved the final manuscript.

Funding

This work was supported by the National Natural Science Foundation of China [Grant number 52067006, 52462053 and 52302470] and the High-end Foreign Expert Talents Project of the Ministry of Science and Technology of China [Grant number G2021022002L].

Declarations

Competing interests

The authors declare no competing interests.

Additional information

Correspondence and requests for materials should be addressed to Y.Y.

Reprints and permissions information is available at www.nature.com/reprints.

Publisher's note Springer Nature remains neutral with regard to jurisdictional claims in published maps and institutional affiliations.

Open Access This article is licensed under a Creative Commons Attribution-NonCommercial-NoDerivatives 4.0 International License, which permits any non-commercial use, sharing, distribution and reproduction in any medium or format, as long as you give appropriate credit to the original author(s) and the source, provide a link to the Creative Commons licence, and indicate if you modified the licensed material. You do not have permission under this licence to share adapted material derived from this article or parts of it. The images or other third party material in this article are included in the article's Creative Commons licence, unless indicated otherwise in a credit line to the material. If material is not included in the article's Creative Commons licence and your intended use is not permitted by statutory regulation or exceeds the permitted use, you will need to obtain permission directly from the copyright holder. To view a copy of this licence, visit <http://creativecommons.org/licenses/by-nc-nd/4.0/>.

© The Author(s) 2025